Materials
Advances

PAPER

Cite this: *Mater. Adv.*, 2026, 7, 5041

Influence of Sm_2O_3 substitution on the mechanical properties, crystallization kinetics, radiation shielding and Judd–Ofelt analysis of borosilicate glasses

Santosh Kumar,[a] Savidh Khan,*[a] Km Abida,[b] F. E. Mansour,[c] R. B. Malidarreh,[d]
H. M. H. Zakaly[d] and A. Saleh[e]

Received 27th February 2026,
Accepted 6th April 2026

DOI: 10.1039/d6ma00278a

rsc.li/materials-advances

Magnesium-containing borosilicate glass samples reinforced with varying concentrations of Sm_2O_3 (0–1.5 mol%) have been produced *via* the conventional melt quenching method in order to investigate the mechanical properties, activation energy of crystallization and transition, thermal stability, fragility index, radiation shielding (MAC, HVL, Z_{eff}, EBAF) and Judd–Ofelt parameters. The X-ray diffraction pattern confirmed the glassy nature of the prepared samples owing to the lack of distinctive X-ray diffraction peaks. The elastic moduli Em and Rm increased from 86.26 to 107.95 GPa and 62.11 to 95.55 GPa, respectively, with an increase in Sm_2O_3 concentration. Crystallization kinetics, especially activation energies (E_g, E_x and E_c), were analyzed *via* the Kissinger and Augis–Bennett methods and were found to increase with increasing Sm_2O_3 concentration. The mass attenuation coefficient (MAC) and the effective atomic number (Z_{eff}) increased, whereas the half-value layer (HVL) decreased as Sm_2O_3 content increased in the glass networks. The MS-1 sample has higher relative photon attenuation efficiency over a broad energy range than the other samples. The Judd–Ofelt parameters follow the same trend ($\Omega_4 > \Omega_2 > \Omega_6$) for all the prepared glass samples. To examine the suitability of Sm^{3+}-substituted borosilicate glass for photonic applications, transition probability (A_r), branching ratio (β_r), radiative lifetime (τ_R), and peak emission cross-section (σ_p) are obtained for each transition band. The examined glasses are promising candidates for laser applications as compared to the other Sm_2O_3 doped glass systems reported in the literature.

1 Introduction

Borosilicate glasses (BSGs) have shown great potential for use in laboratories due to their superior mechanical strength, chemical durability, and exceptional thermal shock resistance as compared to the other glasses, such as borate and soda-lime glasses.[1,2] In the modern era, borosilicate glasses are also explored for solid-state lasers, radiation dosimetry, and radiation shielding applications.[3–5] BSGs have been recognized as good shielding materials owing to their high density and better ionizing radiation absorbability.[6]

Presently, radiation shielding is a primary requirement in radiotherapy, industrial imaging, and aerospace engineering.[7] It is environmentally important, uses radiological facilities and serving as a primary means of safeguarding personnel from exposure risks.[8–10] To optimize gamma radiation shielding, various glasses have been synthesized using high atomic number (Z) compounds to increase their effective atomic number (Z_{eff}) as well as density.[11,12] The light transmission, absorbance, refractive index, and the optical band gap must be rigorously assessed to ensure the suitability of glasses for shielding applications.[9,11,13] For instance, B_2O_3 enhances optical performance, while MgO improves the mechanical and thermal stability. Furthermore, the addition of PbO_2, BaO, TiO_2, GeO_2, TeO_2, *etc.* significantly increases the radiation attenuation abilities of the glasses.[14,15]

Rare earth elements play a vital role in advancing both the gamma radiation shielding and the optical performance of glass materials. Furthermore, the network of glass structure changes with the incorporation of rare earth elements, leading to an increase in density and refractive index, which is essential for superior attenuation efficiency and optical properties.[16] Rare-earth doping significantly enhances luminescence efficiency, enabling advancements in high-performance lighting,

---

[a] Department of Physics and Material Science, Thapar Institute of Engineering and Technology, Patiala-147004, Punjab, India. E-mail: savidhkhan@gmail.com
[b] Department of Chemistry, KVSCOS, Swami Vivekanand Subharti University, Meerut-250005, Uttar Pradesh, India
[c] Department of Physics, College of Science, Qassim University, Buraydah, 51452, Saudi Arabia
[d] Institute of Physics and Technology, Ural Federal University, Ekaterinburg, Russia
[e] Basic Science Department, Higher Technological Institute, 10th of Ramadan City, 228, Egypt

display technologies, and phosphor-based devices. Samarium-doped borosilicate glasses have gained significant attention from the scientific community due to their unique physicochemical properties.[17] Additionally, they are highly suitable for full-color displays and high-density optical memory devices owing to the inherent valence instability of the samarium ion. The interaction between radiation and matter is primarily characterized by the photoelectric effect (0.01–0.5 MeV), photon–electron scattering (>0.5 MeV), and electron–positron pair production (1.02 MeV).[18,19]

Glasses have emerged as an important class of materials for radiation shielding applications.[20] Extensive research has been done on tellurite, borate, phosphate, germanate, and silicate oxides as the primary source of the glass-forming systems.[21] Borate glasses offer a low melting point, high resistance to devitrification, superior density, and effective γ-ray attenuation, particularly in lead-borate compositions, which possess a diverse array of structural units.[22] Concrete is a composite material composed of cement and aggregates such as sand, gravel/crushed stone, and optional additives including supplementary cementitious materials, fibers, and chemical admixtures. In the presence of water, these constituents form a durable material widely used in foundations, bridges, pavements, and buildings. Due to its cost-effectiveness, durability, high mechanical strength, and superior heat resistance, concrete has been widely investigated as a radiation shielding material.[23,24] However, structural degradation, cracking, corrosion, high weight, and environmental concerns related to CO_2 emissions during cement production restrict the use of borate glasses. Ceramics are composed of silica, quartz, and feldspar and exhibit excellent thermal stability, corrosion resistance, hardness, and electrical insulation. These properties make ceramics promising candidates for radiation shielding applications.[23,25] Nevertheless, their inherent brittleness and susceptibility to cracking remain an important limitation.

Furthermore, crystallization kinetics are essential to understand the thermal stability of borosilicate glasses.[26] A differential scanning calorimeter (DSC) is employed to determine the characteristic temperatures of the prepared glasses.[27] The non-isothermal crystallization performance can be effectively characterized using the Augis–Bennett and Kissinger models to estimate the activation energies for crystallization and the glass transition of the prepared glasses.[28,29] Additionally, DSC data are used to assess the Avrami constant (C_e), fragility index (I_f), and Lasocka parameters (X and Y), which provide critical insights into the local structure of the glasses. These factors govern the crystallization kinetics, and optical and mechanical properties of the glasses. Notably, there is always a scarcity of research that systematically correlates crystallization behavior with the mechanical performance of Sm_2O_3-containing borosilicate glasses. UV-Vis-NIR absorption spectra characterize the optical band gap and localized energy states as a result of Sm^{3+} incorporation. The spectral features correspond to electronic transitions within the Sm^{3+} 4f levels, enabling the investigation of the local bonding, structural modifications, and potential radiation-induced defect levels.[30]

The present study determine the effect of Sm_2O_3 substitution on the optical and mechanical properties, crystallization kinetics, and radiation shielding behavior of $50SiO_2 + 40B_2O_3 + (10 - x)MgO + (x)Sm_2O_3$ glass. The mechanical properties are determined using the Makishima–Mackenzie, Rocherulle and bond compression models and correlated to the crystallization kinetics. The unique electronegativity and field strength of MgO and Sm_2O_3 in the glass matrix are responsible for altering the network structure. Therefore, the aim of the present work is to examine the effect of Sm_2O_3 on the non-isothermal crystallization kinetics, mechanical properties, and radiation shielding capability of borosilicate glasses.

Problem statement: borosilicate glasses are widely used in photonic, laser, and radiation shielding applications due to their excellent thermal and chemical stability. However, the performance of these glasses strongly depends on the incorporation of the rare-earth ions, which can modify the glass network structure and influence their optical and mechanical properties. Among the rare-earth ions, Sm^{3+} has attracted considerable attention because of its characteristic orange-red emissions and potential applications in solid-state lasers and photonic devices. Despite several studies on Sm_2O_3-doped glass systems, a comprehensive study on the effect of Sm_2O_3 substitution on the structural rigidity, crystallization behavior, radiation shielding capability, and spectroscopic properties of borosilicate glasses remains limited. Particularly, the influence of Sm_2O_3 on the elastic properties, crystallization kinetics, and Judd–Ofelt parameters of the $SiO_2 + B_2O_3 + MgO$ glass system has not been systematically investigated yet.

Therefore, it is essential to explore the role of Sm_2O_3 substitution in modifying the glass network and the consequent impact on mechanical stability, crystallization resistance, and optical performance. For this purpose, Sm_2O_3-containing borosilicate glass compositions with improved structural and spectroscopic properties for advanced photonic and laser applications are fabricated using the melt and quench method.

Research gap: rare-earth-doped borosilicate glasses have gained significant interest due to their excellent chemical durability, thermal stability, and ability to host optically active ions for applications in photonics and lasers. Among different rare-earth ions, Sm^{3+} is a vital candidate due to its characteristic emission transitions and suitability for solid-state lasers and optical devices. Although several researchers have reported Sm_2O_3-doped phosphate, borate, and silicate glass systems for many applications, a systematic investigation of Sm_2O_3 substitution in MgO-modified borosilicate glass networks remains scarce. In particular, the combined effect of Sm_2O_3 on mechanical properties, crystallization kinetics, radiation shielding behavior, and Judd–Ofelt spectroscopic parameters has not been comprehensively explored in the glass systems.

2 Materials and methods

2.1 Glass synthesis

The glass compositions are prepared using the melt and quenching method according to the general formula

$$50SiO_2 + 40B_2O_3 + (10 - x)MgO + (x)Sm_2O_3 \quad (1)$$

Table 1 Composition in wt% and mol% of Sm_2O_3-containing magnesium borosilicate glasses along with their experimental density

Glass	Elemental composition (wt%)					Oxide composition (mol%)				D_g
ID ↓	Si	B	Mg	Sm	O	SiO_2	B_2O_3	MgO	Sm_2O_3	(g cm^{-3})
MS-0	0.233	0.124	0.060	—	0.581	50	40	10	—	2.32
MS-0.5	0.233	0.124	0.057	0.004	0.580	50	40	9.5	0.5	2.38
MS-1	0.233	0.124	0.054	0.008	0.579	50	40	9	1	2.43
MS-1.5	0.233	0.124	0.051	0.012	0.578	50	40	8.5	1.5	2.48

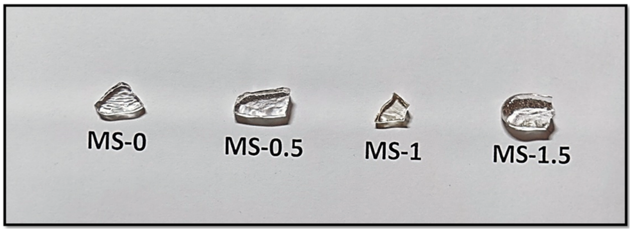

Fig. 1 Photograph of as-synthesized glass samples melted and annealed at 1550 °C and 400 °C, respectively.

where $x = 0$, 0.5, 1, and 1.5 mol%. The selected compositions are given in Table 1. For convenience, the prepared glass samples are nominated as MS-0, MS-0.5, MS-1, and MS-1.5. Sm_2O_3, MgO, B_2O_3 and SiO_2 were weighed using an electronic balance and ground using an agate mortar and pestle. Subsequently, the mixture was placed in a recrystallized alumina crucible and melted at 1550 °C. For homogeneity, the melt was held at 300, 600, 900, 1200, and 1500 °C for 1 hour (h). The melt was then quickly quenched between two copper plates. In the end, the glass samples were annealed at 400 °C for 4 hours. The physical picture of the as-synthesized samples is shown in Fig. 1. It is observed that the bulk density (D_g) increases from 2.32 to 2.48 g cm^{-3} with an increase in samarium ions (Sm^{3+}) at the cost of lighter magnesium ions (Mg^{2+}). It is due to the replacement of lighter magnesium ions (Mg^{2+}) by the heavier samarium ions (Sm^{3+}). In addition, such replacement alters the overall atomic packing density of the glass network.

2.2 Structural and crystallization kinetics study

To analyze the structure of the as-prepared samples, XRD patterns were acquired using a PANalytical X'Pert Pro diffractometer with Cu K_α radiation ($\lambda = 1.54$ Å). The instrument was operated at an accelerating voltage of 40 kV and a current of 30 mA. Diffractograms were recorded in the 2θ range of 10°–90°, with subsequent data processing performed *via* the SmartLab Studio II software package. Differential scanning calorimetry (DSC) was performed using a Linseis PT-1600 high-temperature system. For each measurement, approximately 20 mg of as-prepared powder was placed in a platinum crucible and heated from room temperature to 1000 °C in a nitrogen atmosphere. To analyze the non-isothermal crystallization kinetics of the prepared samples, DSC measurements were done at four different heating rates ($\theta = 10$, 20, 30, and 40 °C min^{-1}) with aluminium oxide (purity = 99.9%) as a reference material. The activation energies are determined using the Kissinger and Augis–Bennett models. Subsequently, the characteristic temperatures and activation energies are used to estimate the Lasocka parameters (A and B), thermal stability (ΔS), fluctuation-free volume (F_v), Avrami's constant (A_c) and the fragility index (F_i).

2.3 Study of mechanical properties using three different models

2.3.1 Makishima–Mackenzie (M–M) approach. The mechanical properties are assessed using the Makishima–Mackenzie, Rocherulle and bond compression models. The Makishima–Mackenzie framework is used to calculate elastic moduli, precisely the Young's modulus (E_m) and other essential mechanical parameters of heavy metal oxide-modified glass materials. This theoretical approach depends on the packing density (P_t) and the dissociation energy of the constituent oxides (D_i). For a multi-component glass system, P_t is determined using the following equation:

$$P_t\ (\mathrm{cm^3\ mol^{-1}}) = \frac{D_g}{M} \times \sum_i x_i P_f \qquad (2)$$

where x_i represents the mole fraction of the ith oxide. P_f denotes the packing factor of the respective oxide constituent (A_pO_q) and is defined according to Makishima as follows:[31]

$$P_f\ (\mathrm{cm^3\ mol^{-1}}) = N_a \times 4.18 \times (pR_A{}^3 + qR_O{}^3) \qquad (3)$$

The symbol D_e represents the total dissociation energy and D_i represents the dissociation energy of constituent oxides per unit volume, expressed in kcal cm^{-3}. The values of D_e for each oxide are taken from the literature which are defined as follows:[31,32]

$$D_e = \sum_i x_i D_i \qquad (4)$$

However, elastic moduli, like the Young's modulus (E_m), shear modulus (K_m) and bulk modulus (R_m), are calculated using the following equations:

$$E_m\ (\mathrm{GPa}) = 83.6 \times P_t \times D_e \qquad (5)$$

$$K_m\ (\mathrm{GPa}) = \frac{30 \times P_t{}^2 \times D_e}{10.2 \times P_t - 1} \qquad (6)$$

$$R_m\ (\mathrm{GPa}) = 10 \times P_t{}^2 \times D_e \qquad (7)$$

$$P_m = 0.5 - \frac{1}{7.2 \times P_t} \qquad (8)$$

where N_a, R_A and R_O, p, q and P_m are Avogadro's number, ionic radius of metal and oxygen, number of metal atoms, number of oxygen atoms, and Poisson's ratio, respectively.[32,33]

2.3.2 Rocherulle model. The Rocherulle model extends the theoretical framework established by Makishima and Mackenzie to evaluate the elastic behavior of the materials. The Rocherulle model introduces an alternative to calculate the packing factor (P_r), accounting for experimental evidence that suggests elastic moduli are independent of glass density.

The total packing density (R_t) is defined as follows:

$$R_t = \sum_i x_i P_r \tag{9}$$

The value of P_r is determined using the following equation:

$$P_r\ \left(\mathrm{cm^3\ mol^{-1}}\right) = N_a \times 4.18 \times \left[\frac{D_g}{M}\right]_{\text{sample}} \times \left(pR_A{}^3 + qR_O{}^3\right) \tag{10}$$

The packing factor (P_r) is determined using the density of the individual constituent oxides rather than the bulk density of the glass sample. Further, similar mechanical properties as defined in the Makishima–Mackenzie approach can be calculated by substituting R_t in place of P_t.

2.3.3 Bond compression model. The bond compression model provides an idea about the quantitative interpretation of the experimental elastic moduli. According to this model, the bulk modulus (B_{bc}) can be written as follows:[34]

$$B_{bc} = \frac{n_b \times r^2 \times \bar{f}}{9} \tag{11}$$

where r represents the bond length between the cation and anion, $\bar{f}$ denotes the average stretching force constant, and n_b signifies the number of network bonds per unit volume of the glass. It is defined as follows:

$$n_b = N_A \times \frac{n_f}{V} \tag{12}$$

Here, N_A represents Avogadro's number, n_f denotes the number of network bonds per glass formula unit, and V signifies the molar volume of the glass. For three-dimensional multicomponent oxide glasses, the parameters B_{bc} and n_b are defined as follows:

$$B_{bc} = \frac{N_A}{9V} \times \sum_i \left(x \times n_f \times \bar{f} \times r^2\right)_i \tag{13}$$

$$n_b = \frac{N_A}{V} \times \sum_i \left(x \times n_f\right)_i \tag{14}$$

Here, x denotes the molar fraction of the constituent oxides. The theoretical Poisson ratio of the multicomponent oxide glass systems can be determined as follows:[34]

$$\sigma_{cal} = 0.28 \times \left(\overline{n_c}\right)^{-0.25} \tag{15}$$

Here, n_c represents the average cross-link density of the glass network, which is defined as follows:

$$\overline{n_c} = \frac{1}{\eta} \times \sum_i (n_c)_i \times (N_c)_i \tag{16}$$

Here, $(n_c)_i$ represents the number of cross-links per cation for the i-th oxide (defined as the number of bridging bonds per cation minus two), $(N_c)_i$ denotes the number of cations per formula unit, and $\sum (x)_i (N_c)_i$ is the total number of cations per glass formula unit. Furthermore, the average atomic ring size (L) for a three-dimensional network structure can be expressed as:[35]

$$B_e = \frac{0.0106 \times \overline{F_b}}{L^{3.84}} \tag{17}$$

Here, $\overline{F_b}$ represents the bond-bending force constant and is assumed to be proportional to the stretching force constant $\bar{F}$ for the first approximation, and B_e denotes the experimental bulk modulus. The stretching force constant $\bar{F}$ of the glass network is expressed as

$$\overline{F} = \frac{\sum \left(x \times n_f \times \overline{f}\right)_i}{\sum \left(x \times n_f\right)_i} \tag{18}$$

2.4 Radiation shielding analysis

2.4.1 MCNP code. Monte Carlo simulations may be used to solve highly complex physical problems. The Monte Carlo simulation code efficiently reproduces the experimental environment by accounting for the geometrical and physical characteristics of the employed equipment, cross-section values, and other databases used in experimental investigations. The literature review demonstrates that the Monte Carlo simulation method is frequently employed to evaluate the radiation shielding characteristics of various glasses.[36,37] Using the Monte Carlo approach, μ/D_g is determined for the prepared glasses. The MCNP5 gamma-ray attenuation setup, which includes several simulation components like the glass sample, a Pb collimator for radiation, a point isotropic source, F4 tally mesh detection field, and Pb blocks to prevent the dispersed radiation, is shown in Fig. 2 as a 3-D image (obtained using Visual Editor VE). The F4 tally at the detection field was positioned at a distance of 70 cm along the same line as the point radiation source, and was used to calculate the average photon flux per MeV cm^2 s^{-1} in the detecting field that passed through the detector. In this simulation, the glass sample was placed 50 cm from the source, between the F4 tally mesh (detection field) and the source. The average photon flux from the glass in the F4 detection field may be obtained by recording each average photon flux from the MCNP5 output file. The Beer–Lambert equation may then be used to determine and show the linear attenuation coefficient. The mass attenuation coefficients in various photon energies were then calculated by dividing each observed linear attenuation coefficient by the glass density. The characteristics of the material determine the structure of the MCNP5 code cell design (the cell structure of the modeled glasses was taken into consideration as a distinct cell in the input file). As a result, for each computation, the cell structure has been characterized as a unique glass sample with varying element mass percentages and densities, as shown in Table 1. When establishing material characteristics using the MCNP5 material card, the mass fractions of each ingredient are considered in accordance with the form criteria of the MCNP5 code. To depict a cell with certain material qualities, the material should then be set to Mn on the material card. The NPS value has been set at 10^8 particles.[38,39] The linear attenuation coefficient (μ, cm^{-3}), which represents the effectiveness of

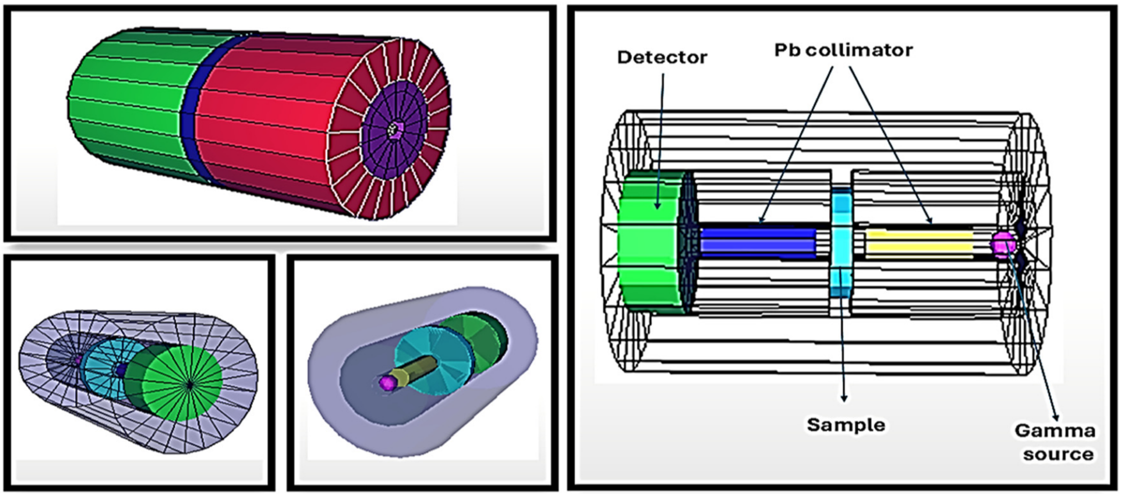

Fig. 2 Gamma photon simulation setup *via* MCNPX visual editor.

shielding materials, can be evaluated using the Beer–Lambert law as shown in eqn (19). Other factors such as the mass attenuation coefficient (MAC) and half value layer (HVL) can be extracted using eqn (20) and (21), where x represent the thickness of the sample in the following equation:[18,40]

$$I = I_0 \times e^{-\mu x} \tag{19}$$

$$\mathrm{MAC}\ (\mathrm{cm^2\,g^{-1}}) = \mu_\mathrm{m} = \frac{\mu}{D_\mathrm{g}} \tag{20}$$

$$\mathrm{HVL} = \varDelta_{0.5}\ (\mathrm{cm^{-1}}) = \frac{0.693}{\mu} \tag{21}$$

2.4.2 Phy-X: PSD software. Complementary shielding parameters, including the effective atomic number (Z_eff), exposure buildup factor (EBF), and energy absorption buildup factor (EABF), are computed using Phy-X: PSD software, which is developed by Sakar *et al.*[41] This is a user-friendly computational tool designed for the rapid evaluation of attenuation factors. The input parameters required for the analysis include elemental compositions, material density, and the gamma photon energy range. The compositions of the candidate composites can be input into the Phy-X: PSD software in either mol percent (mol%) or weight percent (wt%). This software is available for any researcher at https://phy-x.net/.[42]

3 Results and discussion

3.1 X-ray diffraction (XRD) analysis

The XRD patterns of the as-quenched glass samples are illustrated in Fig. 3. The absence of Bragg reflections confirms the amorphous nature of the synthesized samples. Furthermore, the XRD patterns exhibit two diffuse humps at approximately 24° and 45°, which suggests that the incorporation of Sm_2O_3 promotes phase separation in the glass matrix.[43] This diffuse scattering indicates the absence of long-range periodicity in the atomic arrangement, consistent with the presence of short-range order. This structural heterogeneity is attributed to the coexistence of discrete borate and silicate networks.[44] Moreover, the broadening of the hump increases with an increase in Sm_2O_3 concentration, which leads to an increase in glass-forming ability.

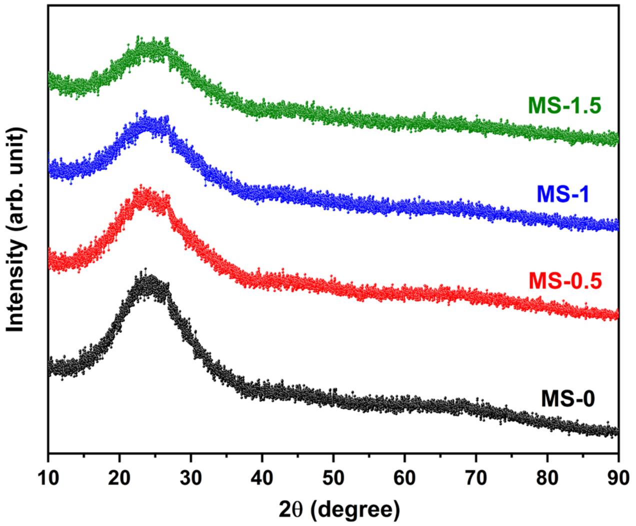

Fig. 3 XRD patterns of the as-prepared $50SiO_2 + 40B_2O_3 + (10 - x)MgO + (x)Sm_2O_3$ series.

3.2 Study of mechanical properties using various models

The study of fundamental structural units of oxide glasses is essential to understand their mechanical properties.[45] However, the relative orientation of adjacent units remains consistent throughout a crystalline lattice, and a random distribution of orientations characterizes a vitreous state.

Table 2 summarizes the crystallographic parameters utilized to calculate the bond compression bulk modulus (B_bc), Poisson's ratio (σ_cal), and the average atomic ring size (L) of the glass samples. The elastic moduli are calculated through the bond compression model (Tables 3 and 4). The experimental

Table 2 Parameters utilised in the calculations are sourced from the corresponding crystal structures of the individual oxides

Oxide ↓	r (Å)	n_f	n_c	$\bar{f}$ (N m^{-1})
SiO_2	1.62	4	2	432
B_2O_3	1.37	3	2	410
MgO	1.82	6	4	282
Sm_2O_3	2.30	6	4	210

Table 3 Calculated values of the average force constant ($\bar{F}$), number of network bonds per unit volume (n_b), average cross-link density ($\overline{n_c}$) and Poisson's ratio (σ_{cal}) for the present glass system

Glass ID ↓	ρ (g cm^{-3})	$\bar{F}$ (N m^{-1})	$n_b \times 10^{28}$ (m^{-3})	($\overline{n_c}$)	σ_{cal}
MS-0	2.32	458.5	7.68	3.39	0.206
MS-0.5	2.38	456.3	7.73	3.41	0.206
MS-1	2.43	453.3	7.75	3.43	0.205
MS-1.5	2.48	451.0	7.77	3.45	0.205

Table 4 Calculated values of the experimental bulk modulus (B_e), bond compression bulk modulus (B_{bc}), ratio (B_{bc}/B_e), and average atomic ring size (L) for the present glass system

Glass ID ↓	B_e (GPa)	B_{bc} (GPa)	B_{bc}/B_e	L (nm)
MS-0	148.01	152.47	1.03	0.410
MS-0.5	149.10	151.74	1.01	0.409
MS-1	149.94	150.74	1.00	0.408
MS-1.5	150.88	149.97	0.99	0.407

Table 5 Calculated elastic moduli (E_m, K_m and R_m), Poisson's ratio (P_m), hardness (V_h), and packing density (P_t) using the Makishima–Mackenzie model of the present samples

	Makishima–Mackenzie (M–M) model					
Glass ID ↓	E_m (GPa)	K_m (GPa)	R_m (GPa)	P_m	V_h (GPa)	P_t (cm^3 mol^{-1})
MS-0	86.26	36.24	62.11	0.269	8.42	0.602
MS-0.5	93.68	38.80	72.83	0.286	8.59	0.650
MS-1	100.80	41.28	83.80	0.300	8.73	0.695
MS-1.5	107.95	43.77	95.55	0.312	8.87	0.740

bulk modulus (B_e) exhibits an increase from 148 to 150 GPa with increasing Sm_2O_3 content. The increase in the bulk modulus is directly proportional to the number of bonds per unit volume (n_b). n_b increases from 7.68 to 7.77 × 10^{28} m^{-3} with the increasing content of Sm_2O_3 from 0 to 1.5 mol%, which is associated with an increase in the mean cross-link density (n_c), as given in Table 3. It signifies improved glass rigidity, as evidenced by the formation of rigid BO_4 units.[46]

Additionally, the B_{bc}/B_e ratio (bond-bending constraints within the network) is directly proportional to the ring diameter (L). The reduction in average ring size (L) from 0.410 to 0.407 nm and B_{bc}/B_e from 1.03 to 0.99 confirms the increased network connectivity.

The mechanical properties of the developed glass samples, particularly stiffness and structural integrity, can be characterized using the packing density, dissociation energy per unit volume, and elastic moduli. To determine these moduli, the Makishima–Mackenzie (M–M) model and the Rocherulle model are employed.[29,47] Both the models help to correlate microscopic characteristics (effects of network formers and modifiers) by providing insights into the local structure configurations of the glasses. The M–M model adopts a macroscopic approach, utilizing experimentally determined bulk density to derive packing density. On the other hand, the Rocherulle model provides a microscopic perspective by calculating the packing density using the molecular weights and densities of the constituent oxides. The calculated elastic moduli (E_m, K_m and R_m) and Poisson's ratio (P_m) are summarized in Table 5. It is observed that the elastic moduli increase (E_m and R_m increase from 86.26 to 107.95 GPa and from 62.11 to 95.55 GPa, respectively) with an increase in Sm_2O_3 concentration, consistent with an increase in the average number of bonds per unit volume and cross-link density. These variations suggest that the stiffness of the glass framework is primarily governed by the nature of the network bonding, especially alterations in cross-linking and coordination as observed in the E_m and R_m trend.[48,49] The transition from BO_3 to BO_4 with the formation of bridging oxygens (BOs) is responsible for enhancing the rigidity and elastic moduli of the present glass samples.[46,50]

The incorporation of Sm_2O_3 into the glass network results in a simultaneous increase in total dissociation energy (D_e) and packing density (P_t), as detailed in Table 7. The rise in D_e and density of network bonds is primarily associated with the high dissociation energy of Sm_2O_3 compared to other constituents.[48,51] As D_e increases, the glass structure becomes progressively more compact, leading to the enhanced elastic moduli as given in Table 5. The present findings indicate that the prepared glass samples possess higher resistance to mechanical deformation. Further, the increase in total packing density and network stiffness is governed by the higher atomic mass, strong bonding between Sm and O and the nature of Sm^{3+} ions compared to other cations in the matrix.[52] Specifically, Sm_2O_3 facilitates higher packing density by enabling ions to occupy interstitial voids within the glass network.

Poisson's ratio (P_m), defined as the ratio of lateral strain to longitudinal strain under an applied tensile force, exhibits a minimal increasing trend from 0.269 to 0.312. According to Souri,[53] loosely packed glass networks permit higher atomic mobility, which lowers the lateral strain. Consequently, P_m tends to increase in more tightly packed structures or *vice versa*. In the present study, the increasing trend of P_m suggests that Sm_2O_3 promotes a more compact network configuration, which is also satisfied by the increasing trend of elastic moduli and structural rigidity.

The theoretical elastic moduli are calculated by using the Rocherulle model as presented in Table 6. The elastic moduli and Poisson's ratio increase with the increase of Sm_2O_3 content. Fig. 4 illustrates the variations in moduli obtained using the Makishima–Mackenzie and Rocherulle models as a function of Sm_2O_3 content. It is noticed that all the elastic moduli show an increasing trend with increasing Sm_2O_3 concentration.

Table 6 Calculated elastic moduli (E_m, K_m and R_m), Poisson's ratio (P_m), hardness (V_h), and packing density (R_t) using the Rocherulle model of the present samples

	Rocherulle model					
Glass ID ↓	E_m (GPa)	K_m (GPa)	R_m (GPa)	P_m	V_h (GPa)	R_t (cm^3 mol^{-1})
MS-0	98.15	40.29	80.42	0.297	8.61	0.685
MS-0.5	102.47	41.81	87.15	0.304	8.72	0.711
MS-1	107.04	43.42	94.49	0.311	8.84	0.738
MS-1.5	111.45	44.98	101.85	0.318	8.91	0.764

To assess the consistency of theoretical frameworks, the relative percentage deviation (R_d) of the Young's modulus is summarized in Table 7. The maximum relative deviation between models was 12.11%, indicating reasonable agreement.

Microhardness (V_h) is defined as the pressure required for eliminating free volume within the glass matrix and it characterizes network deformation. Under high hydrostatic pressure, the glass structure undergoes compaction, reducing free volume. The microhardness was determined using the following expression:[44]

$$V_h = \frac{E_m}{6} \times \frac{(1 - 2 \times P_m)}{(1 + P_m)} \tag{22}$$

Both the models show comparable hardness values that increase with increasing Sm_2O_3 content, attributed to the greater structural contribution of BO_4 units than BO_3 units in the glass network. Thus, it can be concluded that Sm^{3+} ions with relatively high ionic field strength and strong Sm–O bonds are incorporated into the glass network. This leads to an increase in packing density and cross-linking within the borosilicate network, resulting in a more compact and rigid structure. Consequently, the elastic moduli such as the Young's modulus (E_m), bulk modulus (R_m), and shear modulus (K_m) increase with increasing Sm_2O_3 concentration in place of MgO.

3.3 Study of non-isothermal crystallization kinetics

Differential scanning calorimetry (DSC) is employed to study the thermal performance of the glass samples. It provides both qualitative insights into structural changes and quantitative data regarding the characteristic temperatures. The glass transition (T_g), onset crystallization (T_c), and peak crystallization (T_p) temperatures were identified through DSC thermograms. In the DSC thermographs, T_g appears as an endothermic baseline shift, while crystallization and melting are demonstrated as exothermic and endothermic peaks, respectively. Fig. 5 illustrates DSC thermographs at four heating rates (10–40 °C min^{-1}) of the prepared glass samples. T_g was determined from the peak derivative in the DSC peak (DDSC) curve (dH/dT), as shown in Fig. 6, while T_c and T_p were identified through the combined analysis of the slope change and the corresponding DDSC peak.

Table 7 Total dissociation energy (D_e) and relative deviation (R_d) in the Young's modulus (E_m) measured by using the Makishima–Mackenzie and Rocherulle models

	M–M model		Rocherulle model		Relative deviation (R_d)	
Glass ID ↓	P_t	E_m (GPa)	R_t	E_m (GPa)	E_m (%)	D_e (GPa)
MS-0	0.60	86.26	0.68	98.15	12.11	17.14
MS-0.5	0.65	93.68	0.71	102.47	8.57	17.24
MS-1	0.69	100.80	0.73	107.04	5.82	17.35
MS-1.5	0.74	107.95	0.76	111.45	3.14	17.45

The characteristic temperatures of the present glasses exhibit an increase with an increase in heating rates (Table 8), which is associated with the sluggish thermal events in kinetic effects.[54,55] The glass transition is related to the structural relaxation time (t_r) of the material that becomes comparable to the observation time (δT). At a constant heating rate, T_g is governed by the packing density and cross-linkages in the glass structure. T_g depends on the heating rate (α), which arises because T_g is inversely proportional to t_r; a higher heating rate ($\alpha = \delta T/t_r$) reduces the time available for molecular rearrangement, thereby requiring a higher temperature to achieve the transition.[55]

The substitution of Sm_2O_3 in place of MgO facilitates a structural modification in the borosilicate network, promoting

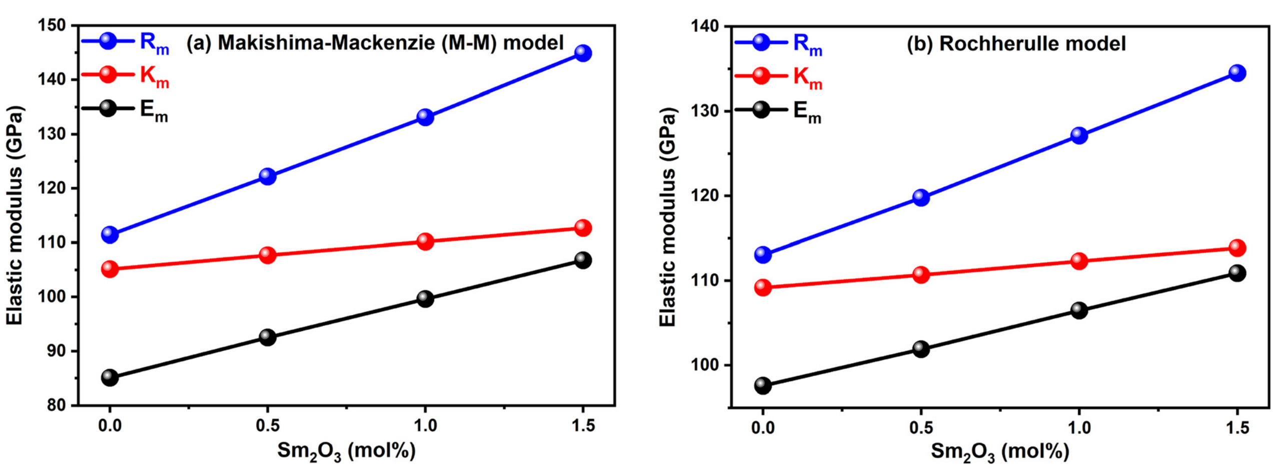

Fig. 4 Variation in elastic moduli (E_m, K_m and R_m) with Sm_2O_3 content (mol%) using (a) the Makishima–Mackenzie model and (b) Rocherulle model.

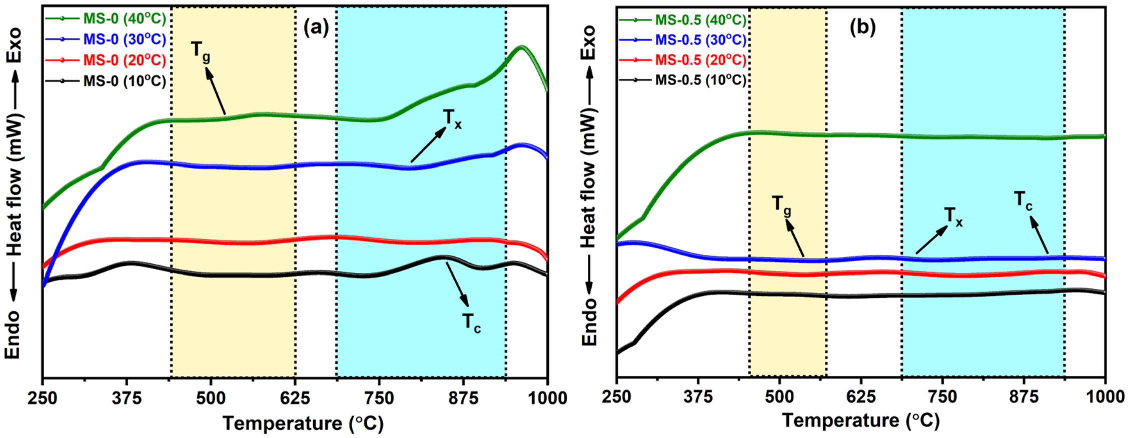

Fig. 5 DSC curves for (a) MS-0 and (b) MS-0.5 obtained at different heating rates.

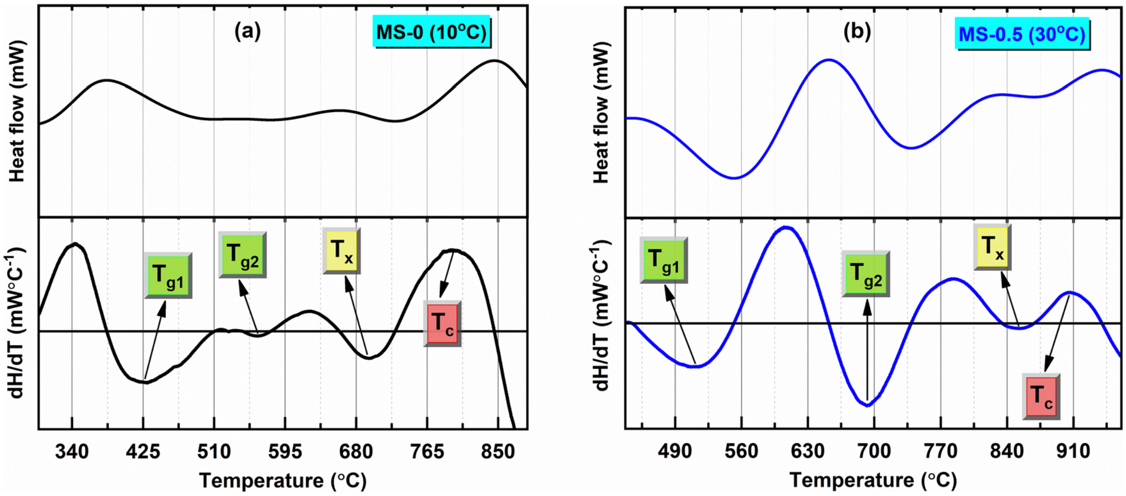

Fig. 6 Derivative curve of differential scanning calorimetry (DDSC) for (a) MS-0 at 10 °C and (b) MS-0.5 at 30 °C.

Table 8 Characteristic temperatures and sintering window (ΔT) of the synthesized glasses at different heating rates

Glass ID ↓	Heating rate (α) (°C min^{-1})	T_{g1} (°C)	T_{g2} (°C)	$\langle T_g \rangle$ (°C)	T_x (°C)	T_c (°C)	$\Delta T = T_c - T_g$ (°C)
MS-0	10	425 ± 1	551 ± 1	488 ± 1	692 ± 1	790 ± 1	302 ± 2
	20	491 ± 1	639 ± 1	565 ± 1	743 ± 1	851 ± 1	386 ± 2
	30	525 ± 1	673 ± 1	599 ± 1	770 ± 1	878 ± 1	279 ± 2
	40	590 ± 1	705 ± 1	647 ± 1	834 ± 1	942 ± 1	295 ± 2
MS-0.5	10	442 ± 1	561 ± 1	501 ± 1	697 ± 1	832 ± 1	331 ± 2
	20	501 ± 1	605 ± 1	553 ± 1	712 ± 1	871 ± 1	318 ± 2
	30	517 ± 1	671 ± 1	594 ± 1	850 ± 1	904 ± 1	310 ± 2
	40	524 ± 1	701 ± 1	612 ± 1	898 ± 1	939 ± 1	327 ± 2
MS-1	10	481 ± 1	595 ± 1	538 ± 1	705 ± 1	869 ± 1	331 ± 2
	20	502 ± 1	670 ± 1	586 ± 1	793 ± 1	873 ± 1	287 ± 2
	30	552 ± 1	727 ± 1	639 ± 1	804 ± 1	879 ± 1	240 ± 2
	40	561 ± 1	740 ± 1	650 ± 1	863 ± 1	919 ± 1	269 ± 2
MS-1.5	10	510 ± 1	632 ± 1	571 ± 1	762 ± 1	875 ± 1	304 ± 2
	20	539 ± 1	649 ± 1	594 ± 1	773 ± 1	896 ± 1	302 ± 2
	30	572 ± 1	662 ± 1	617 ± 1	843 ± 1	908 ± 1	291 ± 2
	40	601 ± 1	673 ± 1	637 ± 1	895 ± 1	951 ± 1	3145 ± 2

the conversion of $Q^4 + Q^2$ into $Q^1 + Q^3$ units.[46] This transition enhances network connectivity and polymerization, resulting in a more connected glass framework. Therefore, a general trend in the characteristic temperatures, *i.e.*, increasing with increasing Sm_2O_3 content, is observed. It supports an increase in thermal stability with increasing Sm_2O_3 content, which is

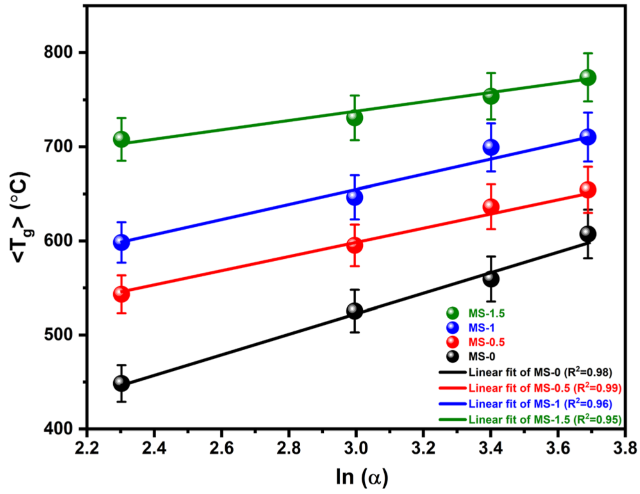

Fig. 7 The Lasocka plot shows the variation of T_g *versus* ln(β) for the as-prepared glasses. A straight line represents the linear fit passing through the data points, with error bars indicating the uncertainty from the linear fitting.

attributed to the shorter bond length, higher cross-link density, and a corresponding increase in overall network rigidity.

3.3.1 Lasocka parameters.

The glass transition temperature ($\langle T_g\rangle$) highly depends on the heating rate (α) and can be expressed as follows:

$$\langle T_g\rangle = X + Y \times \ln(\alpha) \tag{23}$$

The constants X and Y from the Lasocka equation were determined through linear regression of the $\langle T_g\rangle$ *versus* ln(α) plots, as illustrated in Fig. 7. The constant X represents the glass transition temperature extrapolated to a heating rate of 1 °C min^{-1}, while Y is a configurational constant sensitive to the glass composition and quenching rate. Y is governed by the cooling rate and decreases with slower cooling rates. The specific values derived from the intercept (X) and slope (Y) are listed in Table 9. The incorporation of Sm_2O_3 into the SiO_2–B_2O_3–MgO glass system is responsible for the systematic decrease in X (459.88 to 231.84 K). Conversely, Y increases with an increase in Sm_2O_3 content, suggesting that the MS-1.5 sample undergoes greater configurational modifications. The inverse relationship in X and Y for MS-1.5 glass indicates better resistance to devitrification.[46] Additionally, enhanced stability is supported by the higher activation energy, as discussed in the subsequent sections.

Table 9 Lasocka parameters and the frequency factor (ν) for as-prepared samples

	Lasocka parameter		
Glass ID ↓	X	Y	ν (s^{-1})
MS-0	459.88	46.77	5.24 × 10^{31}
MS-0.5	311.62	81.80	8.91 × 10^{17}
MS-1	340.08	84.97	5.49 × 10^{15}
MS-1.5	231.84	110.71	1.20 × 10^{13}

3.3.2 Crystallization activation energy.

Glass initially undergoes a glass transition on heating, followed by crystallization to form a glass-ceramic material.[56] The nucleation and growth phenomena occur during the crystallization process. It is governed by the network connectivity, chemical composition, viscosity, and the free energy difference between the phases. Glass transition and crystallization processes are kinetically controlled phenomena that proceed only when the available thermal energy is sufficient to overcome their respective activation energy barriers. To understand the barriers in the present glass samples, two distinct mathematical models were employed to determine the activation energies associated with glass transition and crystallization events. According to the Kissinger model,[57] the activation energy for the glass transition is derived from the T_g and heating rate (α) as follows:

$$\ln\frac{\langle T_g{}^2\rangle}{\alpha} = \frac{E_g}{R\langle T_g\rangle} + C \tag{24}$$

In the above equation, C, E_g, and R are the constant, activation energy of the glass transition, and the universal gas constant, respectively. As illustrated in Fig. 8(a), the plot of $1000/\langle T_g\rangle$ and $\ln(\langle T_g{}^2\rangle/\alpha)$ exhibits a linear trend, where the slope is utilized to calculate the activation energy (E_g) for all samples. The data are well fitted by linear regression, and the obtained E_g values are summarized in Table 10. Error bars (2%) are included to specify the uncertainty associated with the linear fitting process.

In the Augis–Bennett model, the relationship between the heating rate (α) and the glass transition temperature ($\langle T_g\rangle$) is defined as follows:

$$\ln\frac{\langle T_g\rangle}{\alpha} = \frac{E_g}{R\langle T_g\rangle} + C \tag{25}$$

Fig. 8(b) illustrates the plots of $\ln(\langle T_g\rangle/\alpha)$ *versus* $1000/\langle T_g\rangle$ for all glass samples. The Kissinger model is adapted to determine the crystallization activation energy by substituting the glass transition parameters (T_g and E_g) with the crystallization temperatures (T_x or T_c) and activation energies (E_x or E_c), respectively. The crystallization activation energy (E_c) and the frequency factor (ν) are evaluated using the Augis–Bennett model as follows:

$$\ln\frac{T_x}{\alpha} = \frac{E_x}{R \times T_x} - \ln\nu \tag{26}$$

The crystallization activation energies (E_x and E_c) are determined through graphical analysis using the Kissinger and Augis–Bennett models, as illustrated in Fig. 9 and 10, respectively. The calculated E_x and E_c values are summarized in Table 10. E_c represents the energy barrier that must be overcome for the glass-to-crystal transition. Thus, higher E_c values signify greater resistance to devitrification with enhanced thermal stability. The activation energies derived from the Kissinger and Augis–Bennett models have strong agreement, with minor discrepancies attributable to the distinct underlying assumptions of each framework. The reliability of the results is supported by an excellent correlation coefficient (R^2) of 0.99. The Augis–Bennett model can determine the frequency factor (ν).

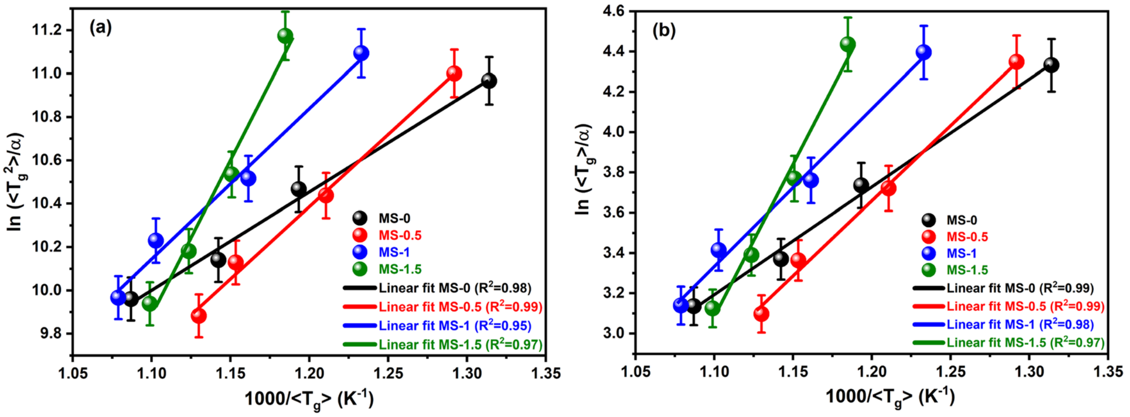

Fig. 8 Activation energy of crystallization (E_g) of as-prepared glasses using the (a) Kissinger model and (b) Augis–Bennett model.

Table 10 obtained values of E_g, E_c and E_r for the as-prepared samples

	Kissinger model			Augis–Bennett model		
Glass ID ↓	E_g (kJ mol^{-1})	E_x (kJ mol^{-1})	E_c (kJ mol^{-1})	E_g (kJ mol^{-1})	E_x (kJ mol^{-1})	E_c (kJ mol^{-1})
MS-0	38	65	107	45	73	110
MS-0.5	55	71	133	62	85	143
MS-1	87	89	161	95	98	179
MS-1.5	118	119	333	127	136	348

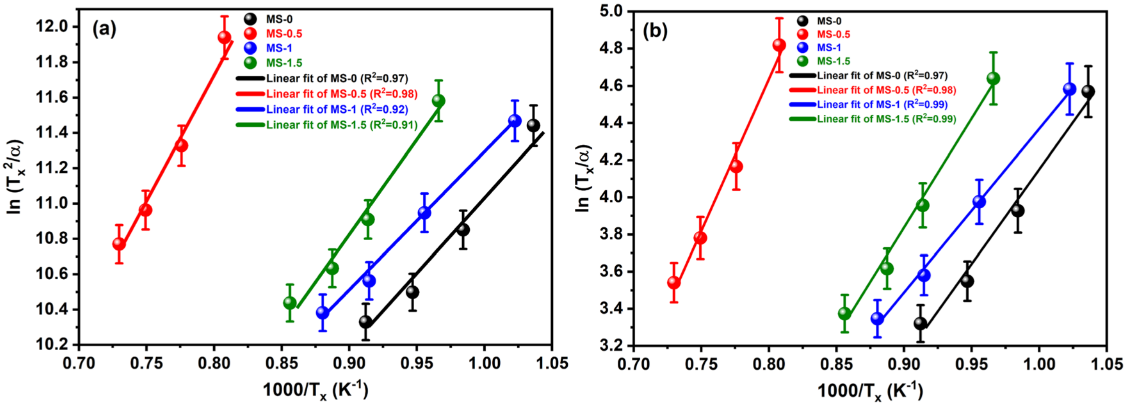

Fig. 9 Activation energy of crystallization (E_g) of as-prepared glasses using the (a) Kissinger model and (b) Augis–Bennett model.

The obtained values of the frequency factor are given in Table 9. It represents the atomic attempt frequency required to surmount the crystallization barrier and provides critical insights into the availability of nucleation sites in the glass network.[47,58] Consequently, ν serves as an essential parameter for assessing the overall stability of the glass samples. Both models consistently reveal a linear trend in E_x and E_c, *i.e.*, increasing with an increase in Sm_2O_3 content. Notably, the MS-0 sample exhibits minimum E_c and maximum ν values, signifying a higher tendency for crystallization facilitated by an elevated atomic attempt frequency. On the other hand, the MS-1.5 sample exhibits the highest E_c and the lowest ν, indicating greater thermal stability against devitrification compared to the other glass samples. This stability can be associated with the more uniform network structure that requires higher energy for atomic rearrangement. So, it can be concluded that the incorporation of Sm_2O_3 increases the activation energy by modifying the network connectivity with enhanced structural integrity of the borosilicate framework. Thus, it can be concluded that the Kissinger and Augis–Bennett models show an increase in crystallization activation energy (E_c) with increasing Sm_2O_3 concentration. This behavior suggests that Sm^{3+} ions suppress crystallization by hindering atomic diffusion and structural rearrangement in the glass matrix.

3.4 Avrami constant

The shape of the DSC crystallization peak provides essential information regarding the crystallization mechanism in glass samples. The sharp exothermic peaks indicate bulk crystallization, whereas broader peaks indicate surface crystallization.[59] The full width at half maxima (FWHM; ΔT_w) quantifies peak broadening.

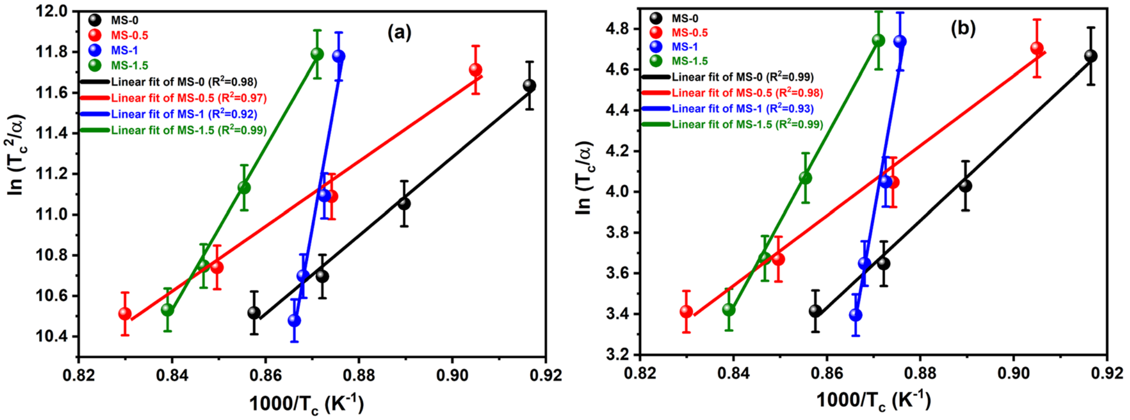

Fig. 10 Activation energy of crystallization (E_g) of as-prepared glasses using the (a) Kissinger model and (b) Augis–Bennett model.

Consequently, the Avrami constant (C_A), which characterizes the dimensionality and mechanism of crystallization, can be determined using ΔT_w and activation energy (E_c) according to the following expression:[60]

$$C_A = \frac{2.5}{\Delta T_w} \times \frac{R \times \langle T_g \rangle^2}{E_g} \tag{27}$$

The Avrami constant (C_A), typically ranging from 1 to 4, is a key parameter for interpreting the crystallization mechanism. When $C_A = 3$, it signifies bulk crystallization consistent with the sharp exothermic peaks observed in the DSC thermographs. When $C_A = 1$, it indicates surface-mediated crystallization. The heating rate also affects the Avrami constant because the heating rate (α) significantly influences the peak shape as shown in Table 11. It is observed that C_A increases from 10 to 40 °C min^{-1} as α increases. It is also noticed that C_A increases with increasing Sm_2O_3 content, which suggests that the substitution of Sm_2O_3 promotes bulk crystallization in the present glass samples. Generally, a higher C_A reflects a stronger tendency toward volume-nucleated, multidimensional growth.[61]

3.4.1 Fluctuation free volume. The fluctuation-free volume (V_f) is an important parameter for studying the structural changes that govern glass kinetics during the glass transition and crystallization. Higher values of V_f indicate a more open network that facilitates atomic movement and structural rearrangements. The assessment of V_f is crucial for correlating network connectivity and plays a fundamental role in determining the overall mechanical and thermal stability of the glass samples. The fluctuation-free volume is calculated using the following expression:

$$V_f = \frac{8.314 \times \langle T_g \rangle}{E_g} \tag{28}$$

Table 11 Various kinetic parameters of the as-prepared glasses at different heating rates

Glass ID ↓	θ (°C min^{-1})	C_A	$V_f \times 10^{-3}$	I_f	ΔS (°C)
MS-0	10	1.20	90.16	4.81	60.64
	20	1.59	104.38	4.16	73.78
	30	2.70	110.66	3.92	50.30
	40	3.86	119.53	3.63	49.24
MS-0.5	10	1.76	67.18	6.46	89.19
	20	2.69	74.15	5.85	91.43
	30	2.46	79.65	5.45	28.18
	40	3.62	82.06	5.29	21.90
MS-1	10	1.81	47.08	9.22	100.89
	20	2.37	51.28	8.47	39.18
	30	3.34	55.92	7.76	281.6
	40	4.67	56.88	7.63	23.17
MS-1.5	10	2.76	37.38	11.62	60.16
	20	3.13	38.88	11.17	62.53
	30	3.79	40.39	10.75	30.65
	40	4.15	41.70	10.41	27.60

The obtained fluctuation-free volume (V_f) reveals the significant structural modifications in the glass network, with a clear heating rate and Sm_2O_3 concentration dependency. V_f decreases as the heating rate increases from 10 to 40 °C min^{-1} as given in Table 11. This phenomenon suggests that a higher heating rate provides sufficient time for the glass network to reach thermodynamic equilibrium, thereby trapping less free volume. This excess free volume helps structural modifications and higher atomic mobility.[47] Further, the substitution of MgO with Sm_2O_3 in the borosilicate glass leads to a decrease in V_f. This trend validates the role of Sm_2O_3 as a network former, which enhances the borosilicate glass network by forming Si–O–B linkages and generating BOs. The resultant structure is more compact, less expandable, and less flexible. The minimal V_f of the MS-1.5 glass indicates a highly compact and rigid network, whereas the higher of V_f in the MS-0 glass reflects a more disordered configuration. This structural modification is consistent with the observed trend in the crystallization activation energy (E_c), where low V_f corresponds to high E_c, thereby confirming that Sm_2O_3 enhances the overall network rigidity. From a functional perspective, the dense network associated with the low V_f typically enhances mechanical robustness and chemical durability. Conversely, the more open network characterized by high V_f facilitates ionic transport and may control the optical characteristics. Therefore, the incorporation of Sm_2O_3 supports tuning the physical and chemical properties of these borosilicate glasses.

3.4.2 Fragility index. The fragility index of glass-forming liquids classifies them as either kinetically "strong" or "fragile".

Kinetically strong liquids typically exhibit substantial covalent character with discrete coordination, resulting in a well-defined network structure. Conversely, kinetically fragile liquids are often derived from simple molecular fluids with isotropic coordination and are characterized by ionic or van der Waals forces.[62]

The glass transition temperature ($\langle T_g \rangle$) is conventionally defined as the temperature at which the liquid's viscosity (η) abruptly increases to 10^{12} Pa s. However, this definition is not universally applicable, as certain molecular liquids exhibit viscosities below 10^{10} Pa s at the glass transition. To address such a discrepancy, Angell introduced the concept of fragility, in which the logarithm of viscosity is plotted against the inverse normalized temperature ($\langle T_g \rangle/T$). In this case, strong glass formers (SiO_2) display Arrhenius temperature dependency, whereas fragile glass formers (*ortho*-terphenyl) exhibit distinct non-Arrhenius behavior. Furthermore, fragile structures are known to undergo rapid structural degradation near the glass transition.[63] Consequently, the kinetics of the glass transition are quantified by the fragility index (I_f), which is most commonly defined by the slope of the viscosity curve as it approaches T_g on an Angell plot.

$$I_f = \lim_{T \to \langle T_g \rangle} \frac{d(\log_{10} \eta)}{d(\langle T_g \rangle / T)} \tag{29}$$

Upon incorporating V_f, eqn (29) simplifies to

$$I_f = \frac{1}{V_f \times 2.302} \tag{30}$$

The fragility index (I_f) serves as a key indicator of glass-forming kinetics. Kinetically strong (KS) melts typically exhibit an I_f value near 16. Traditional glass formers such as SiO_2, GeO_2, P_2O_5, and As_2O_3 generally fall within the range of 17 to 20, but B_2O_3 is an exception at approximately 32.[62,64] Conversely, kinetically fragile (KF) melts display significantly higher values, approaching 200.[48] Table 11 represents the fragility indices of the prepared glass samples. The values range from 4.81 to 11.62, indicating that these compositions possess a favorable glass-forming ability consistent with kinetically strong characteristics. It is observed that glasses with higher Sm_2O_3 content exhibit higher fragility indices, which can be attributed to the interactions between borate and silicate structural units. In addition, the fragility index decreases with increasing heating rates. Finally, glass fragility is intrinsically linked to composition and bond topology, as modifications in local structural environments allow different regions to relax at different heating rates, resulting in a broad distribution of relaxation times.

3.4.3 Thermal stability.

To evaluate the feasible processing window and resistance to devitrification of Sm_2O_3 modified $SiO_2{-}B_2O_3{-}MgO$ glasses, thermal stability is assessed using the working range (ΔS) and the Saad stability factor (ΔS). The working range ($\Delta T = T_c - \langle T_g \rangle$) represents the temperature interval available for processing before the onset of crystallization. A larger ΔT value indicates enhanced thermal stability. Further, the Saad stability parameter (ΔS) provides an additional quantitative measure of this stability and is calculated as follows:

$$\Delta S = \frac{(T_c - T_x) \times \Delta T}{\langle T_g \rangle} \tag{31}$$

The Saad stability factor (ΔS) analysis identifies an optimal Sm_2O_3 concentration for maximizing the thermal resistance of the glass system. The 1 mol% Sm_2O_3-doped sample (MS-1) demonstrates higher thermal stability, achieving a peak ΔS value of 100.89 as shown in Table 11. This enhancement is attributed to the formation of robust Si–O–B bonds, which increase network cross-linking and reduce the density of NBOs. On the other hand, the 1.5 mol% Sm_2O_3-doped sample (MS-1.5) exhibits the lowest stability (ΔS = 60.16), suggesting that the excessive Sm_2O_3 amount disrupts the glass network and promotes NBO formation. The undoped (MS-0) and 1 mol% Sm_2O_3 samples (MS-1) display intermediate stability, with values ranging from 60.64 to 49.24 and from 100.89 to 23.17, respectively. These findings highlight the need for proper optimization of Sm_2O_3 to tune thermal performance. Thus, MS-1 is identified as the most suitable glass for high-temperature processing and long-term applications in optoelectronics, solid-state devices, and protective coatings.

3.5 Gamma photon radiation shielding study

MAC serves as a vital parameter to study the radiation shielding capability of the materials based on the per-unit-mass. The incident gamma-photon energy and density of the glass matrix predominantly influence the behavior of materials. The MAC values show a pronounced decrease with an increase in gamma-photon energy, which is associated with the dominant gamma-photon interaction mechanisms (photoelectric (PE), Compton scattering (CS), and pair production (PP)) as shown in Fig. 11.[65] Generally, density and MAC show an inverse relationship, which can be attributed to the substitution of

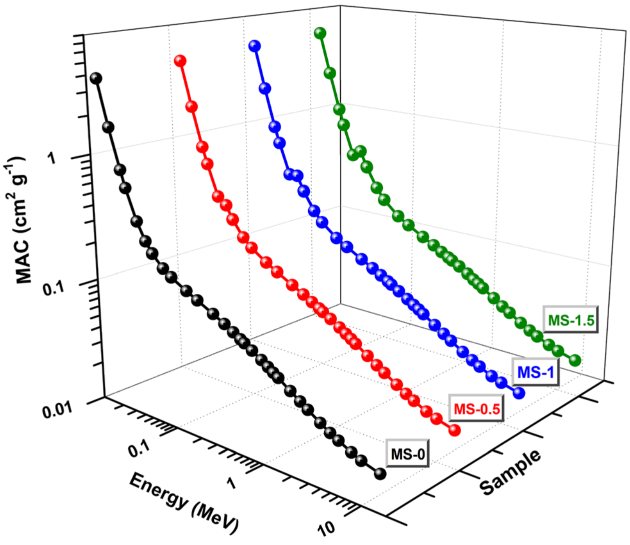

Fig. 11 MAC values as a function of gamma photon energy for the MS series.

MgO with Sm_2O_3 in glass samples. The incorporation of Sm_2O_3 improves the interaction cross-section, which leads to a change in the attenuation properties. Additionally, a distinct K-edge absorption feature centered around 48.6 keV is produced by increasing Sm_2O_3 content. This feature becomes more prominent with higher Sm_2O_3 content. Further, the increment in MAC values can be attributed to the higher effective atomic number and density introduced by Sm^{3+} ions, which increases the probability of photon interaction, particularly through the photoelectric effect at low photon energies. Fig. 12 and 13 depict the partial contributions of individual gamma-photon interaction mechanisms and their respective average percentages to the total MAC for the MS-0 sample across a broad gamma-photon energy range. Different patterns of interaction are observed with different energy domains. Precisely, the photoelectric effect (PE) dominates in the lower energy range, exhibiting a pronounced decline as gamma-photon energy increases.[65] In contrast, the Compton scattering (CS) curve demonstrates a more gradual attenuation across the energy range. Rayleigh (coherent) scattering exhibits a nearly linear decreasing trend. The photoelectric effect is predominant in the lower energy range (0.015 to 0.3 MeV). The CS interaction dominates between 0.4 and 8 MeV and approaches 98% significance, while the PE is found at nearly 80% in the effective range (Fig. 13). At higher energies (between 10 and 15 MeV), a comparable trend is observed, with a prominent increase in the pair production (PP) interaction. It is attributed to its inverse-square dependence on gamma-photon energy, which governs the elastic scattering behavior of gamma-photons. The MAC values fall in the range of 1.95×10^{-2} to 3.93 (for MS-0) and 0.0199 to 4.98 (for MS-1.5) at 0.015 and 15 MeV, respectively. Overall, the relative contribution of each interaction is strongly influenced by both the gamma-photon energy and the compositions. The HVL denotes the material thickness necessary to reduce the incident gamma-photon intensity by 50%. It has a strong dependency on gamma-photon energy, which is associated with the gamma-photon–matter interaction mechanisms that vary across different energy regimes. The PE is dominant in the range of 10–100 keV and the HVL reveals a steep relationship with E (directly proportional to E^3). In the case of CS between 100 and 1000 keV, the HVL exhibits a linear relationship with E, as shown in Fig. 14. On the other hand, in a high-energy zone where PP dominates ($E > 1.022$ MeV), the HVL follows an approximate inverse logarithmic trend with E ($\ln(E^{-1})$). This behaviour in the PP region occurs due to the high atomic number (Z) of materials.[37,66] Due to the overlapping energy dependence of PE and CS interactions, HVL values in the low and intermediate energy regions tend to converge closely. However, a more distinguishable gradient in HVL values is observed with an increase in the PP domain. Beyond the energy dependence, the HVL is also influenced by the composition of the shielding materials. At a constant gamma-photon energy, variations in material constituents yield different HVL values. For instance, at 10 MeV, the HVL spans

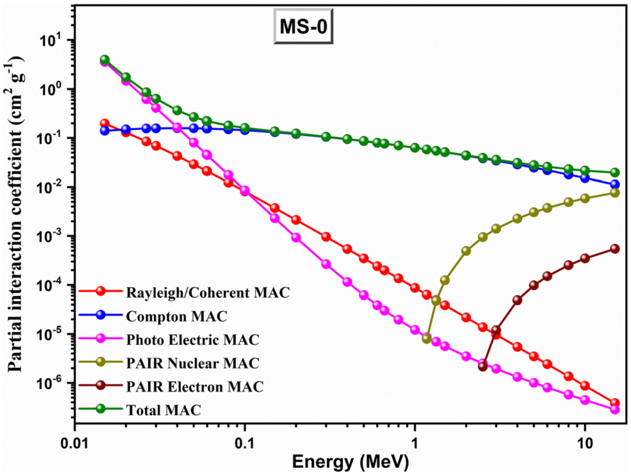

Fig. 12 Partial interaction contributions to the total MAC *vs.* gamma photon energy for the MS-0 sample.

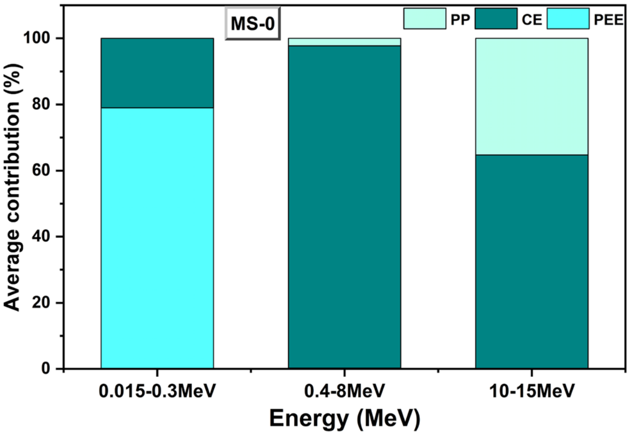

Fig. 13 The average percentage contribution of PE absorption, CS and PP to the total MAC related to the MS-0 sample for 3 different gamma photon energy ranges.

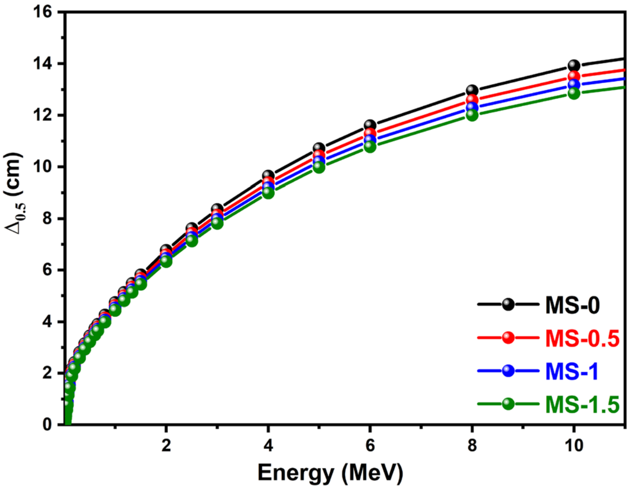

Fig. 14 $\Delta_{0.5}$ fluctuations for the provided samples as a function of gamma photon energy.

from 13.3 cm in MS-0 to 12.1 cm in MS-1.5, indicating superior attenuation performance in the latter. These findings suggest that MS-1.5 exhibits enhanced gamma-photon radiation shielding efficiency, characterized by the lowest HVL across the evaluated energy spectrum (0.001 eV to 10 MeV).[66]

Fig. 15 illustrates the energy dependence of the effective atomic number (Z_{eff}) of the prepared glass samples. As energy increases, it is observed that Z_{eff} first decreases, then rises sharply, and finally gradually attenuates. The undoped glass sample (MS-0) exhibits a smooth, monotonic decrease, while Sm_2O_3-containing samples exhibit distinct, sharper maxima. This is attributed to the K-edge absorption of Sm^{3+}, occurring near 46.8 keV, which induces a localized surge in photon interaction probability.[66] Increased inner-shell electron interactions, particularly in the PE absorption regime, are responsible for the observed peak. The CS-dominant interaction mechanism causes Z_{eff} to resume a downward trajectory beyond this energy threshold, and the impact of PE absorption diminishes. Z_{eff} is more sensitive to the composition due to the presence of high atomic number dopants such as Sm_2O_3. Even minor additions of Sm^{3+} significantly enhance Z_{eff}, especially within the photon energy range corresponding to the K-edge. Furthermore, the dependence of Z_{eff} on compositional variation is inherently nonlinear. The incorporation of rare-earth elements introduces a non-proportional enhancement in Z_{eff}, underscoring the complex interplay between elemental concentration and photon interaction cross-sections. As demonstrated in Fig. 15, low-weight fractions of Sm_2O_3 induce a substantial increase in Z_{eff} in the vicinity of the absorption edge. At higher photon energy levels, the Z_{eff} curves exhibit minimal deviation. Nevertheless, the undoped glass sample exhibits the lowest gamma-ray attenuation efficiency, while the Sm^{3+} containing glass sample shows superior shielding capability over a broad energy range.[66]

In addition, the figure shows that Z_{eff} values range from 8.43 to 11.2 (for MS-0) and from 8.5 to 15.4 (for MS-1.5). RPE% is the capacity of materials to attenuate ionizing radiation. Within the low-energy photon domain, a notable gradient in RPE% is observed, whereas in the intermediate- and high-energy regions, the curves are converged and approach zero, indicating minimal shielding differentiation at elevated energies. It is observed that RPE% is intrinsically governed by the density and composition. The incorporation of high atomic number (Z) additives into the glass matrix significantly improved the attenuation performance. As Sm_2O_3 content increases, the shielding capacity of the prepared glass samples increases.[37] Furthermore, a strong positive correlation is established between gamma-photon attenuation and the corresponding RPE values, supporting that materials exhibiting higher photon interaction probabilities provide superior radiation mitigation. The MS-1.5 sample shows the highest radiation shielding efficiency across a broad energy spectrum compared to the other glass samples, as shown in Fig. 16. In addition, the MS-0 sample achieves 100% protection till 0.02 MeV while the MS-1.5 sample achieves 100% protection till 0.0263 MeV. In addition to this, the increasing trend of RPE with Sm_2O_3 concentration is due to the absorption of a greater fraction of incident gamma photons. The improvement in RPE is mainly associated with the increased photon interaction cross-section and the enhanced stopping power resulting from the higher atomic number of Sm.

The EBF quantifies the accumulation of scattered radiation within a shielding material. Fig. 19 and 20 illustrate the energy-dependent performance of EBF of the prepared glass samples. The dependency of EBF on material density reflects a multifaceted interaction influenced by incident photon energy, depth of penetration, and composition of the glass, particularly Z_{eff}. It is observed that the relationship between EBF and photon energy is inherently nonlinear, exhibiting a pronounced maximum at intermediate energy levels, followed by a decline at both lower and higher energies. This intermediate-energy behavior is attributed to the compositional makeup of the synthesized glass matrices. Precisely, an increase in Sm^{3+}

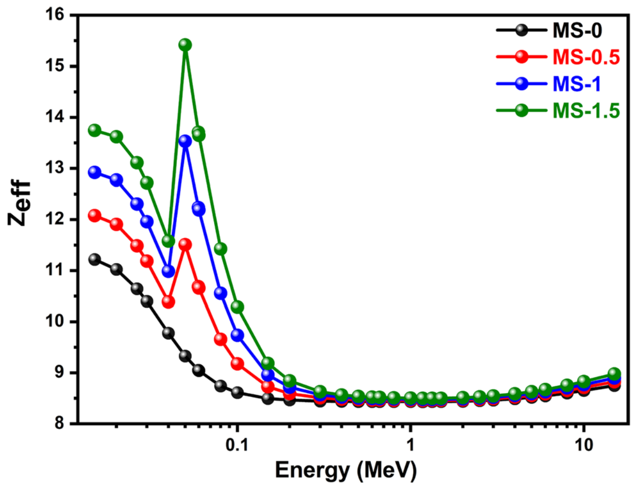

Fig. 15 Variation of Z_{eff} with gamma photon energy for the MS series.

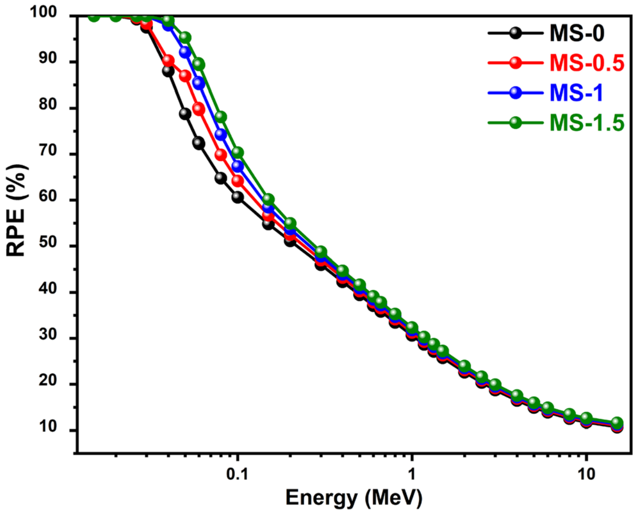

Fig. 16 Variations of evaluated RPE for the selected samples with photon energy.

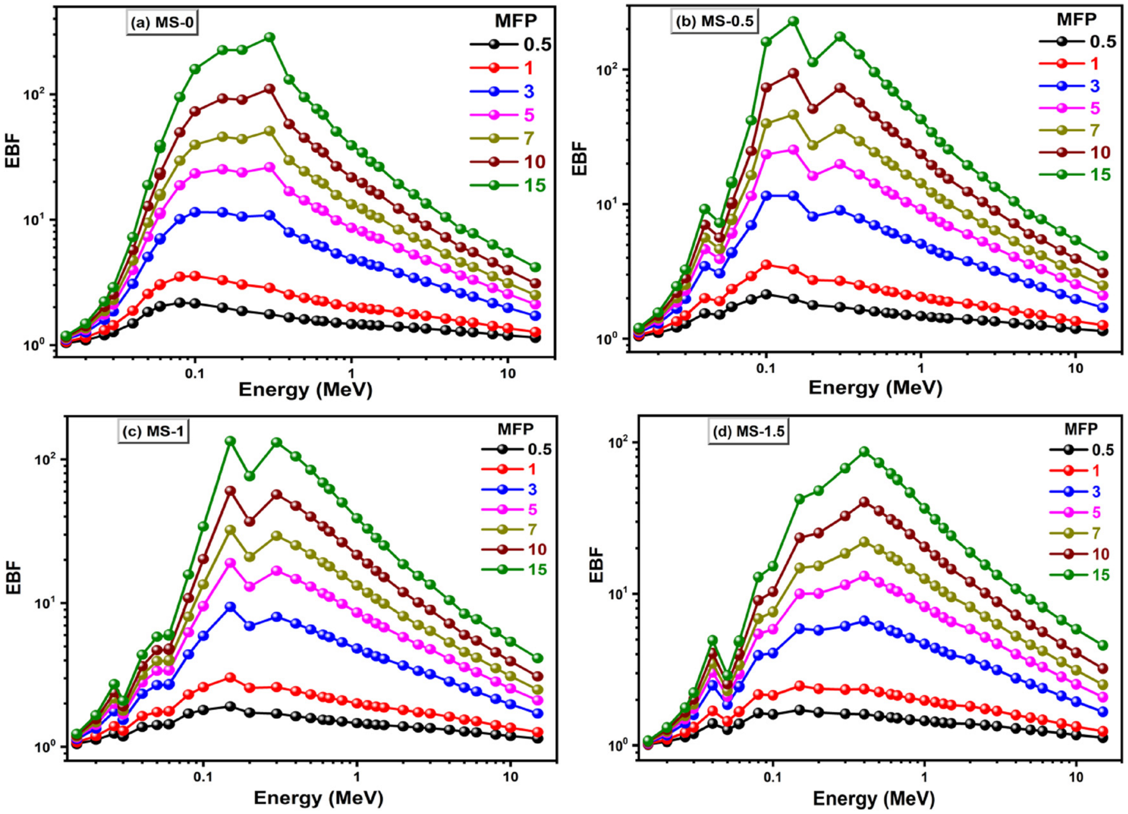

Fig. 17 EBF *versus* gamma photon energy at different penetration depths for all investigated samples.

concentration is accompanied by a reduction in Mg^{2+} content, resulting in pronounced peaks. This phenomenon arises due to the substitution of a high-*Z* element (Sm^{3+}) for a low-*Z* element (Mg^{2+}).[37] Moreover, the composition alteration enhances the probability of photoelectric interactions. It is evident, particularly by the sharp peaks near 46.8 keV in the PE region, as the Sm^{3+} concentration increases. Conversely, the occurrence of broader peaks around 1305 keV is associated with reduced Mg^{2+} content. These variations could also result from elemental substitution-induced changes in material density. Additionally, at a penetration depth of 15 mfp, the prepared glass samples demonstrate comparable behavior, with variations in EBF magnitude correlating to differences in the atomic structure and bulk density of the glass matrix. The same trend is also reported for EABF for the prepared glass samples – a parameter used to quantify how gamma-photons are absorbed and scattered within the materials in the wide energy ranges – as shown in Fig. 17 and 18. As expected, at fixed mfp, the EABF follows the trend $EABF_{1.5} < EABF_1 < EABF_{0.5} < EABF_0$. The MS-1.5 sample has the lowest EBF and EABF values, while the MS-0 sample possesses the highest values. The EABF values slightly decrease with increasing Sm_2O_3 concentration at most photon energies. This reduction suggests that photon penetration and multiple scattering inside the material become less significant as the glass becomes more effective at attenuating photons. The presence of heavier Sm^{3+} ions increases the probability of photon absorption before multiple scattering events occur.

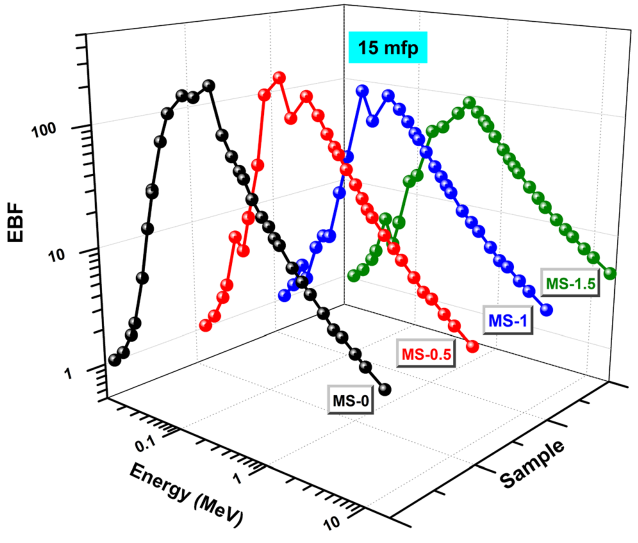

Fig. 18 Variations of the EBF for the MS series as a function of gamma photon energy at a penetration depth of 15 mfp.

The energy dependency of the kerma relative to air (K_α) of the prepared glass samples is shown in Fig. 21. Kerma is a measure of energy transferred from radiation to matter and is maximum for the MS-1.5 glass sample in a wide energy range. This indicates that the MS-1.5 sample has the highest value of kinetic energy released per unit mass compared to the other

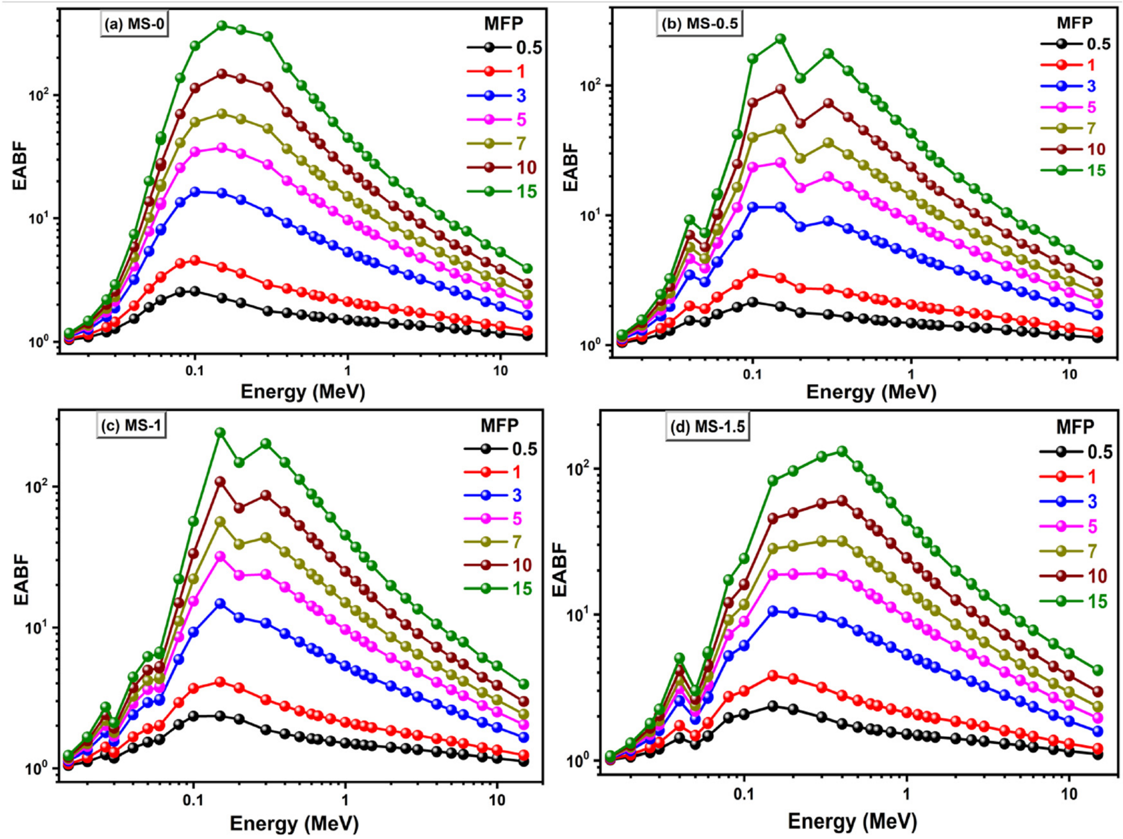

Fig. 19 EABF values *versus* gamma photon energy at different penetration depths for the MS series.

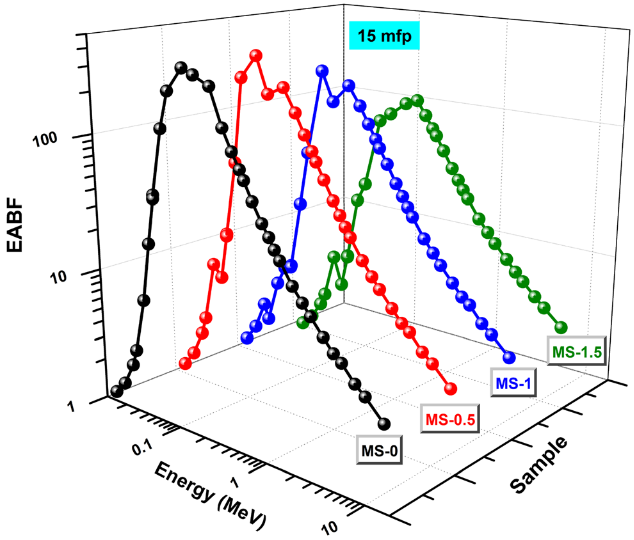

Fig. 20 Changes of EABF values for the MS series as a function of gamma photon energy at a penetration depth of 15 mfp.

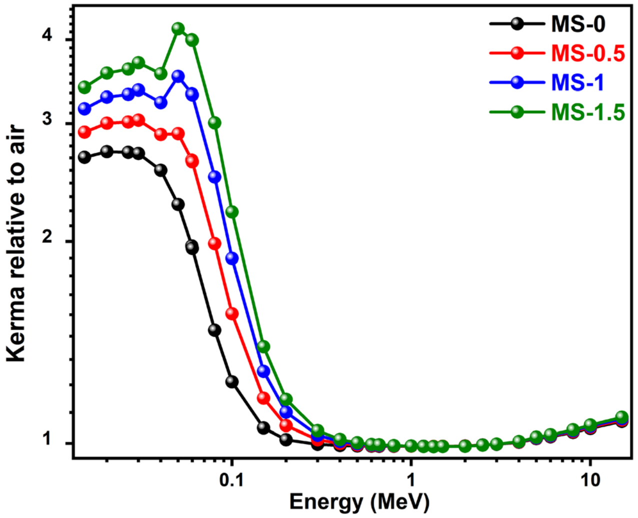

Fig. 21 The change of K_α of the present samples as a function of gamma photon energy.

samples.[67] On the other hand, the gamma-photon loss in the MS-0 glass sample is small due to its lowest K_α. Furthermore, the MS-1.5 sample shows a sharp peak due to the higher Sm^{3+} content. Moreover, a descending trend in K_α is seen due to the increasing Sm^{3+} content as follows: $K_{\alpha(\text{MS-0})} < K_{\alpha(\text{MS-0.5})} < K_{\alpha(\text{MS-1})} < K_{\alpha(\text{MS-1.5})}$.

The gamma-photon dose rate (D_r) has been quantitatively assessed for the prepared glass samples and illustrated in Fig. 22 and 23. The data indicate that the increase in sample

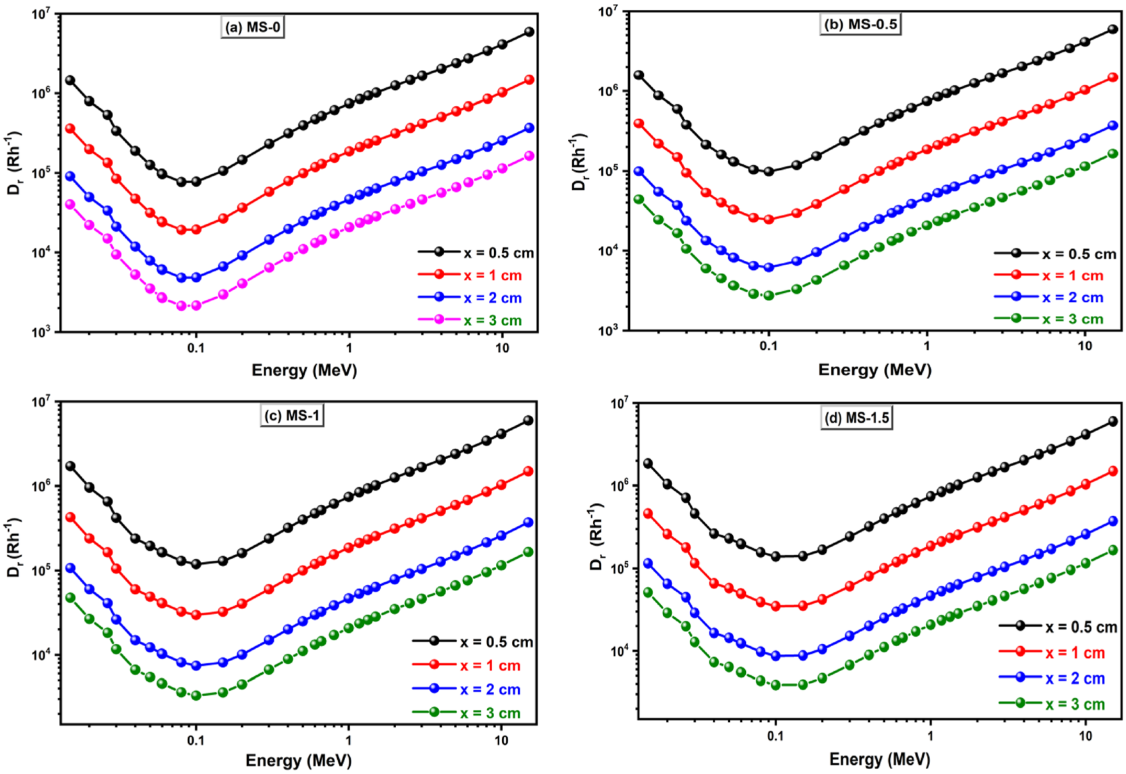

Fig. 22 D_r variation for the prepared samples as a function of gamma photon energy.

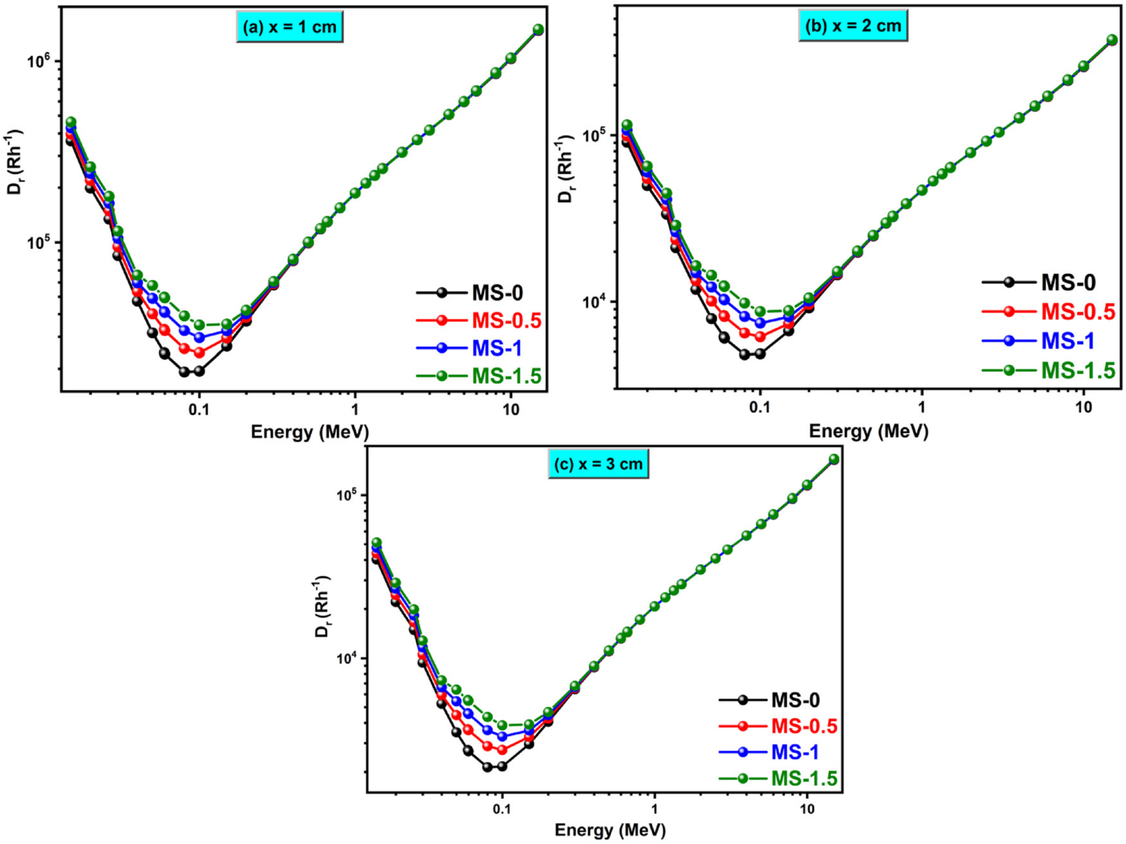

Fig. 23 D_r variation for the prepared samples as a function of gamma photon energy at different thicknesses.

Table 12 Comparison of radiation shielding parameters of Sm_2O_3-doped or rare-earth doped glass systems at 0.662 MeV

Glass ID ↓	MAC ($cm^2\ g^{-1}$)	HVL (cm)	Z_{eff}	Ref.
MS-0	0.63	0.46	10.40	Present work
MS-0.5	0.69	0.42	11.18	Present work
MS-1	0.74	0.38	11.96	Present work
MS-1.5	0.80	0.34	12.71	Present work
Sm_2O_3 containing borate	7.4–8.1	0.040–0.046	32–35	68
$PbO-B_2O_3-SiO_2-Sm_2O_3$	8.35	0.041	33.8	65
La_2O_3/Nd_2O_3 containing borate	6.72	0.052	30–32	69
Sm_2O_3 contain borate	0.19–1.44	1.02–2.72	—	70

thickness (denoted as x) leads to a corresponding decrease in D_r. This trend is consistently observed across all glass samples, typically exhibiting a distinct valley in the low-energy region. As thickness increases further, the respective D_r curves converge, suggesting the potential for graphical overlap. This convergence indicates reduced differentiation in shielding response at higher thickness levels. Furthermore, replacing high-Z Sm_2O_3 with MgO increases density and modifies the structural network, which improves D_r performance. For fixed thicknesses, the attenuation valleys become smooth with increasing Sm_2O_3 content, highlighting the critical influence of composition and density variation on radiation interaction performance. At elevated thicknesses, these valleys tend to vanish completely, resulting in a linearized response curve. This observation suggests the appearance of a near-linear relationship of thickness with D_r, reinforcing the dominant role of physical and chemical parameters in modulating shielding efficiency. The present results of radiation shielding are compared with the existing literature on Sm_2O_3-containing samples in Table 12.

3.6 Study of oscillator strengths and Judd–Ofelt intensity parameters

Fig. 24 represents the absorbance spectra of the prepared glass samples in the wavelength range of 250–1250 nm. The absorbance bands are observed at 402, 475, 941, 1075, and 1219 nm wavelengths, which are assigned to $^6H_{5/2} \rightarrow {}^6P_{3/2}$, $^6H_{5/2} \rightarrow {}^4I_{11/2}$, $^6H_{5/2} \rightarrow {}^6F_{11/2}$, $^6H_{5/2} \rightarrow {}^6F_{9/2}$ and $^6H_{5/2} \rightarrow {}^6F_{7/2}$, respectively. The nephelauxetic ratio (N_r) is a vital parameter to identify the nature of the bond between metal and ligands. It is obtained by dividing the examined wavenumber of the as-quenched glass (ν_c) by the wavenumber of the concerned transition of an aqua ion (ν_a). The energies of concerned transitions (ν_c), average nephelauxetic ratios $\left(\overline{N_r}\right)$, and bonding parameters (B_p) corresponding to the different transitions are determined and presented in Table 13. The relationship between $\overline{N_r}$ and the bonding parameter (B_p) can be written as follows:

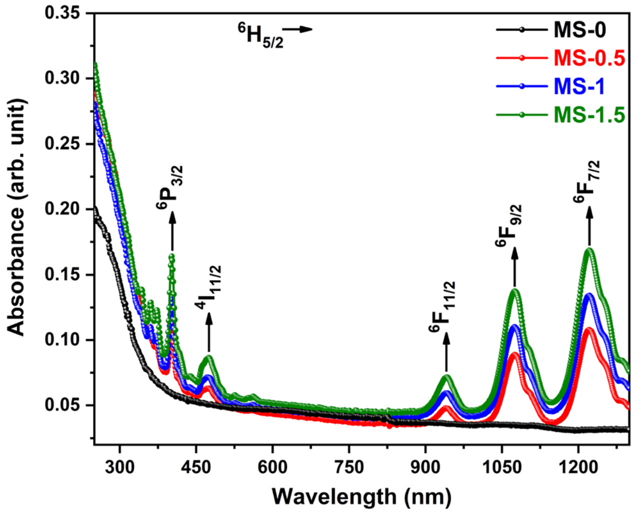

Fig. 24 UV-Visible NIR absorption spectra of Sm_2O_3-containing magnesium borosilicate glasses.

Table 13 The energy of concerned transition (ν_c), average nephelauxetic ratios $\left(\overline{N_r}\right)$, and bonding parameters (B_p) of as-prepared glasses

	ν_c (cm^{-1})		
Transition ↓	MS-0.5	MS-1	MS-1.5
$^6H_{5/2} \rightarrow {}^6P_{3/2}$	24875.62	24937.65	24937.65
$^6H_{5/2} \rightarrow {}^4I_{11/2}$	21052.63	21097.04	21052.63
$^6H_{5/2} \rightarrow {}^6F_{11/2}$	10626.99	10626.99	10638.29
$^6H_{5/2} \rightarrow {}^6F_{9/2}$	9302.32	9310.98	9319.66
$^6H_{5/2} \rightarrow {}^6F_{7/2}$	8203.44	8196.72	8196.72
$\overline{N_r}$	1.010	1.011	1.011
B_p	−0.991	−1.083	−1.082

$$B_p = \frac{1 - \overline{N_r}}{\overline{N_r}} \times 100 \tag{32}$$

The average nephelauxetic ratios are greater than 1 $\left(\overline{N_r} > 1\right)$, and bonding parameters are less than zero ($B_p < 0$), which signifies more inter-electronic repulsions in metal–ligand bonds. Thus, it confirms the presence of ionic bonding between the Sm^{3+} ions and ligands in the prepared glasses.

The absorption ability is measured in terms of oscillator strength. The experimental oscillator strength (f_{exp}) and calculated oscillator strength (f_{cal}) are determined using the $^6H_{5/2} \rightarrow {}^6P_{3/2}$, $^6H_{5/2} \rightarrow {}^4I_{11/2}$, $^6H_{5/2} \rightarrow {}^6F_{11/2}$, $^6H_{5/2} \rightarrow {}^6F_{9/2}$ and $^6H_{5/2} \rightarrow {}^6F_{7/2}$ transitions. The experimental oscillator strength can be calculated as follows:

$$f_{exp} = \frac{4.318 \times 10^{-9}}{S \times R} \int A(\bar{\nu}) \times d\bar{\nu} \tag{33}$$

where $A = \log(I/I_0)$ is the absorbance at wavenumber $\bar{\nu}$, S is the

Table 14 experimental oscillator strength ($f_{exp} \times 10^{-6}$), calculated oscillator strength ($f_{cal} \times 10^{-6}$) and root-mean-square value (δ_{rms}) of as-prepared glasses

	MS-0.5		MS-1		MS-1.5	
Transition ↓	f_{exp}	f_{cal}	f_{exp}	f_{cal}	f_{exp}	f_{cal}
$^6H_{5/2} \rightarrow {}^6P_{3/2}$	0.467	0.789	2.804	2.214	0.137	0.931
$^6H_{5/2} \rightarrow {}^4I_{11/2}$	0.048	0.012	0.663	0.113	0.858	0.012
$^6H_{5/2} \rightarrow {}^6F_{11/2}$	1.792	0.943	3.421	3.385	0.392	0.985
$^6H_{5/2} \rightarrow {}^6F_{9/2}$	3.971	5.497	7.471	10.354	3.921	5.756
$^6H_{5/2} \rightarrow {}^6F_{7/2}$	7.268	6.286	10.894	9.336	7.916	6.587
δ_{rms} ($\times 10^{-6}$)	0.91		1.51		1.17	

rare-earth ion concentration in mol l^{-1} and R is the thickness of the material. The calculated oscillator strength of transition between the lowest level ψ_J and the excited level ψ'_J of the samarium ion is determined using the following equation:[78]

$$f_{cal} = \frac{8\pi^2 mS}{3h} \times \frac{\left(p^2+2\right)^2}{9p} \times \frac{\bar{\nu}}{2J+1} \sum_{\alpha=2,4,6} \Omega_\alpha \langle \psi_J \| U^\alpha \| \psi_{J'} \rangle^2 \tag{34}$$

where ν denotes the wavenumber of a transition, h is the Planck's constant, p is the refractive index, and Ω_α (α = 2, 4 and 6) are Judd–Ofelt (J–O) parameters. These parameters can be obtained by standard least-squares fitting of f_{exp} and f_{cal}. J and J' are the total angular momentum of the ground state and upper state, and $\left|\langle \psi_J \| U^\alpha \| \psi'_J \rangle\right|^2$ signifies the doubly reduced matrix element of a unit tensor operator. The matrix elements are taken from the literature.

The obtained values of f_{exp} and f_{cal} are depicted in Table 14. It is revealed that the experimental oscillator strength (f_{exp}) and the calculated oscillator strength (f_{cal}) show approximately close agreement with each other, which is further confirmed by the root-mean-square value. The root-mean-square value (δ_{rms}) is determined by the following relation:[79]

$$\delta_{rms} = \sqrt{\frac{\sum \left(f_{exp} - f_{cal}\right)^2}{N}} \tag{35}$$

The smaller value of δ_{rms} represents the good fitting between the experimental oscillator strength (f_{exp}) and the calculated oscillator strength (f_{cal}). Therefore, it is assigned to the validity of Judd–Ofelt parameters of the prepared glass materials.

Brian R. Judd[80] and George S. Ofelt[81] introduced a theory to understand the glass structure and radiative behavior of rare-earth-ion-activated materials. They examined Ω_2, Ω_4, and Ω_6 parameters, which are known as Judd–Ofelt parameters. The Ω_2 parameter confirms the symmetry as well as the covalent nature of the Sm–O bond. The Ω_4 and Ω_6 parameters are associated with the rigidity and viscosity of a material, respectively. The obtained values of Judd–Ofelt parameters are listed in Table 14. It is noticed that Ω_4 attains a higher value than other parameters in all the prepared glass samples, which signifies the existence of better rigidity in all the prepared glasses. In the present report, the synthesized glasses follow the $\Omega_4 > \Omega_2 > \Omega_6$ trend, which signifies the excellent rigidity and lack of covalent nature.[17]

Further, the spectroscopic quality factor (χ) is calculated by dividing Ω_4 by the Ω_6 parameter. The obtained quality factors of MS-0.5, MS-1, and MS-1.5 glass samples are 1.10, 1.64, and 1.68, respectively. The present results are compared with the existing literature on Sm^{3+}-doped samples (Table 15). It is observed that the MS-1.5 glass sample has a higher spectroscopic quality factor than others, which leads to a better ability in stimulated emission.

3.7 Radiative properties

The probability of a radiative transition from an excited state to a subordinate energy level is computed as follows:

$$B(\psi_K, \psi_{K'}) = B_p + B_q \tag{36}$$

where B_p and B_q denote the transition probabilities associated with electric and magnetic dipole interactions, respectively. These parameters are determined using the following expressions:[82]

$$B_p = \frac{64\pi^4 e^2 \bar{\nu}^3}{3h(2J+1)} \times \frac{p\left(p^2+2\right)^2}{9} \sum_{\alpha=2,4,6} \Omega_\alpha \langle \psi_K \| U^\alpha \| \psi_{K'} \rangle^2 \tag{37}$$

$$B_q = \frac{64\pi^4 e^2 \bar{\nu}^3}{3h(2J+1)} \times p^3 \frac{\hbar^2}{4m^2 S^2} \sum_{\alpha=2,4,6} \Omega_\alpha \langle \psi_K \| L+2S \| \psi_{K'} \rangle^2 \tag{38}$$

The matrix elements $\langle \psi_K \| U^\alpha \| \psi_{K'} \rangle^2$ and $\langle \psi_K \| L+2S \| \psi_{K'} \rangle^2$ are evaluated within the intermediate coupling scheme, where $\| U^\alpha \|$ signifies the reduced matrix element of the unit tensor

Table 15 The values of Ω_2, Ω_4 and Ω_6 (10^{-20} cm^2), trend of Judd–Ofelt (J–O) parameters, and spectroscopic quality factor (χ) of as-prepared glasses

Glass ID ↓	Ω_2	Ω_4	Ω_6	Trend	χ	Ref.
MS-0.5	3.72	3.93	3.58	$\Omega_4 > \Omega_2 > \Omega_6$	1.10	Present work
MS-1	3.98	4.02	2.45	$\Omega_4 > \Omega_2 > \Omega_6$	1.64	Present work
MS-1.5	4.10	4.69	2.80	$\Omega_4 > \Omega_2 > \Omega_6$	1.68	Present work
FTe1	1.33	1.40	1.14	$\Omega_4 > \Omega_2 > \Omega_6$	1.22	71
Te1	1.16	1.28	1.03	$\Omega_4 > \Omega_2 > \Omega_6$	1.24	71
Sm^{3+} doped borate	2.39	4.71	6.53	$\Omega_4 > \Omega_6 > \Omega_2$	0.72	70
Sm^{3+} doped fluorophosphate	0.98	1.97	1.45	$\Omega_4 > \Omega_6 > \Omega_2$	1.35	72
LBTAF	0.27	2.52	2.47	$\Omega_4 > \Omega_6 > \Omega_2$	1.02	73
CNGS	1.26	3.52	3.44	$\Omega_4 > \Omega_6 > \Omega_2$	1.02	74
Sm^{3+} doped Li_2O–B_2O_3	0.38	3.01	2.01	$\Omega_4 > \Omega_6 > \Omega_2$	1.49	75
Sm^{3+}:BPWLTe	2.62	4.64	2.91	$\Omega_4 > \Omega_6 > \Omega_2$	1.59	76
F30	1.66	2.55	1.56	$\Omega_4 > \Omega_2 > \Omega_6$	1.63	77

Table 16 Radiative transition probability (B), total radiative transition probability (B_T), decay time (τ_R), branching ratio (β_R) and stimulated emission cross section (σ_p ($\times10^{-22}$ cm^2)) parameters of as-prepared glasses

Glass ID ↓	Transitions ($^4G_{5/2}\rightarrow$)	λ_p (nm)	A_r (s^{-1})	A_T (s^{-1})	τ_R (ms)	β_R	σ_p
MS-0.5	$^6H_{5/2}$	548	607.97	1633.08	0.61	0.65	4.28
	$^6H_{7/2}$	600	535.01			0.24	1.06
	$^6H_{9/2}$	645	490.09			0.11	1.03
MS-1	$^6H_{5/2}$	548	619.96	1659.80	0.60	0.66	4.42
	$^6H_{7/2}$	600	552.14			0.24	1.21
	$^6H_{9/2}$	646	487.70			0.10	1.18
MS-1.5	$^6H_{5/2}$	548	647.43	1723.13	0.58	0.69	4.89
	$^6H_{7/2}$	600	555.14			0.25	1.52
	$^6H_{9/2}$	646	520.54			0.06	1.44

operator. These values are taken from the existing literature. Therefore, the total radiative transition probability (B_S) for the excited state is obtained by aggregating the probabilities across all available decay channels, as follows:

$$B_S = \sum B(\psi_K, \psi_{K'}) \tag{39}$$

The branching ratio provides a measure of the relative intensity distribution among the diverse emission pathways originating from a given excited state. It is defined as follows:

$$\beta_R = \frac{B(\psi_J, \psi_{J'})}{B_T} \tag{40}$$

Among the observed transitions, the $^4G_{5/2} \rightarrow {}^6H_{5/2}$ transition exhibits the highest branching ratio than others, suggesting its potential for laser oscillation. The experimental branching ratios (β_R) confirm the predominance of blue emission, following the hierarchical order ($^6H_{5/2} > {}^6H_{7/2} > {}^6H_{9/2}$) as given in Table 16, which suggests that MS-1.5 glass is a suitable candidate for visible orange-red laser applications. Furthermore, the radiative lifetime (τ_R) of the excited state is defined as being inversely proportional to the total radiative transition probability ($1/B_T$).

The Judd–Ofelt parameters are used to evaluate radiative properties such as the branching ratio (β_R), decay time (τ_R), and radiative and total radiative transition probabilities (A_r and A_T) for the exciting level of Sm^{3+} ions in the prepared glass samples. The obtained values of radiative parameters are presented in Table 16. The emission at 548, 600, and 648 nm corresponds to the $^4G_{5/2} \rightarrow {}^6H_{5/2}$, $^4G_{5/2} \rightarrow {}^6H_{7/2}$, and $^4G_{5/2} \rightarrow {}^6H_{9/2}$ transitions, respectively. The $^4G_{5/2} \rightarrow {}^6H_{5/2}$ transition attains a higher radiative transition probability than other possible transitions. As Sm_2O_3 increases, the total radiative transition probability increases from 1633.080 to 1723.135 s^{-1}. The decay times of MS-0.5, MS-1, and MS-1.5 glass samples are 0.61, 0.60, and 0.58 ms, respectively. The present findings signify that samarium oxide in the glass matrix plays a vital role in improving radiative emission. The present results of decay time and stimulated emission cross section are compared with the existing literature on Sm_2O_3-doped samples in Table 17.

The branching ratio is the most significant parameter of stimulated emission. Notably, the β_R parameter has a higher value than 0.50 (50%) in all the prepared glass samples. The MS-1.5 glass has the highest value for all transitions as compared to the other glass samples. Moreover, the stimulated emission cross-section (σ_p) is calculated as shown in Table 16. The $^4G_{5/2} \rightarrow {}^6H_{5/2}$ transition has a higher value of the σ_p parameter compared to the other transitions. The stimulated emission cross-section increases with increasing Sm_2O_3 concentration. Therefore, the high Ω_2, Ω_4/Ω_6 ratio, σ_p and τ_R values (Tables 15 and 17) of the Sm^{3+} doped glasses as compared to the existing literature make them suitable for laser and photonic applications.

Table 17 Comparison of stimulated emission cross section (σ_p ($\times10^{-22}$ cm^2)) and decay time (τ_R) of Sm_2O_3-doped glass systems with existing literature

Glass ID ↓	σ_p ($^4G_{5/2} \rightarrow {}^6H_{7/2}$)	τ_R (ms)	Ref.
MS-0.5	1.06	0.61	Present work
MS-1	1.21	0.60	Present work
MS-1.5	1.52	1.68	Present work
Sm^{3+} doped Li_2O–B_2O_3	2.95	0.65–1.62	75
Sm^{3+}:BPWLTe	1.69	0.64	76
SmWZnBTe	5.36	1.17	74

4 Conclusion

A novel glass system with the formula $50SiO_2 + 40B_2O_3 + (10 - x)MgO + (x)Sm_2O_3$ (x = 0 to 1.5 mol%) was successfully synthesized *via* the conventional melt-quenching method. Increasing Sm_2O_3 doping introduced multifunctional enhancement across mechanical, thermal, optical, and radiation shielding properties of the borosilicate glasses.

- Density increased from 2.32 g cm^{-3} (MS-0) to 2.48 g cm^{-3} (MS-1.5) due to the substitution of heavier Sm^{3+} ions, which confirms a dense and more compact glass network.
- XRD confirmed the amorphous nature of all compositions.
- Elastic moduli such as the Young's, shear, and bulk modulus exhibited an increasing trend with Sm_2O_3 concentration, reflecting enhanced rigidity and mechanical integrity of the glass structure. These enhancements are associated with stronger Sm–O bonds that reinforce the borosilicate network.
- The glass transition temperature ($\langle T_g \rangle$) increased from 488 °C (MS-0) to 571 °C (MS-1.5). Thermal stability ($\Delta T = T_c - T_g$) increased from 302 °C to 331 °C, indicating better resistance to devitrification and higher structural integrity.
- The increasing trend of the Avrami constant from 1.20 to 2.76 with Sm_2O_3 substitution indicates that bulk crystallization dominates in the as-prepared glass samples.
- The Judd–Ofelt intensity parameters increased with increasing Sm_2O_3 content, indicating enhanced asymmetry and rigidity around the Sm^{3+} ions within the glass matrix.
- The mass attenuation coefficient (MAC) decreased significantly with increasing gamma photon energy, consistent with the prevailing photon interaction mechanisms. The MS-1 sample exhibited the highest relative photon attenuation efficiency (RPE) over a broad energy range as compared to the other samples. The exposure buildup factor (EABF) followed the trend $EABF_{1.5} < EABF_1 < EABF_{0.5} < EABF_0$. The kerma

relative to air followed the order $K_{\alpha(\text{MS-0})} < K_{\alpha(\text{MS-0.5})} < K_{\alpha(\text{MS-1})} < K_{\alpha(\text{MS-1.5})}$.

Overall, the incorporation of Sm_2O_3 significantly enhances the structural compactness, mechanical rigidity, radiation attenuation capability, and luminescence efficiency of SiO_2–B_2O_3–MgO glasses. Among all compositions, the MS-1.5 sample consistently exhibited superior performance across most evaluated parameters, indicating its potential for multifunctional applications in photonics and radiation shielding.

5 Novelty of the study

The present research establishes a systematic investigation into the multifunctional development of rare-earth-modified borosilicate glasses. Precisely, it explores the Sm_2O_3 incorporation (0 to 1.5 mol%) effect on a tailored $50SiO_2 + 40B_2O_3 + (10 - x)MgO + (x)Sm_2O_3$ host matrix. The novelty of the present study is as follows:

- Comprehensive structure–property correlation: the present study provides a detailed understanding of the effect of Sm^{3+} ions on structural and active radiative/non-radiative centers.
- Advanced compositional optimization: the systematic distribution of Sm_2O_3 modifies the structure, thermal stability, and optical properties. This approach permits the fine-tuning of material properties while strictly preserving the amorphous integrity and phase homogeneity of the glass matrix.
- Synergistic integration of radiation shielding and photonic properties: the present research reports a correlation between photoluminescence efficiency and gamma-radiation attenuation with an increase in Sm_2O_3 content at the cost of MgO. The findings establish that MS-1.5 glass is a high-performance, dual-functional candidate for advanced solid-state lighting and radiation protection in nuclear and aerospace environments.
- Sm_2O_3-mediated structural reconstruction: Minimal Sm_2O_3 incorporation affects substantial network polymerization and structural rigidity. This transition is driven by the higher field strength of Sm^{3+} ions, which leads to an increase in the hardness as well as the elastic modulus. This structural evolution is validated through different theoretical models, *i.e.*, Makishima–Mackenzie, Rocherulle and the bond compression model.

Conflicts of interest

No conflicts of interest exaist to disclose.

Data availability

Data will be made available on request.

Acknowledgements

This research did not receive dedicated funding from public, commercial, or non-profit organisations. Financial assistance for this project was provided by the Thapar Institute of Engineering and Technology (TIET), Patiala. The authors would like to express their gratitude to DST-TIET for granting access to characterisation facilities through the FIST-II scheme.

References

1 A. Madheshiya, C. Gautam and S. Upadhyay, Preparation, optical and electrical properties of bismuth substituted lead titanate borosilicate glass and glass ceramics, *J. Non-Cryst. Solids*, 2018, **502**, 118–127.

2 S. Kumar, K. Singh and D. Kumar, SiO_2/B_2O_3 glass formers effect on transparency and mechanical properties of soda-lime borosilicate glasses for automobile applications, *J. Non-Cryst. Solids*, 2023, **618**, 122530.

3 M. H. A. Mhareb, M. Alqahtani, Y. Alajerami, F. Alshahri, M. Sayyed, K. Mahmoud, N. Saleh, N. Alonizan, M. Al-Buriahi and K. M. Kaky, Ionizing radiation shielding features for titanium borosilicate glass modified with different concentrations of barium oxide, *Mater. Chem. Phys.*, 2021, **272**, 125047.

4 M. Mhareb, M. A. Morsy, H. Almarri, M. Sayyed, I. Alrammah, N. Alonizan, Y. Alajerami, Q. Drmosh, M. K. Hamad and G. N. Makhadmeh, *et al.*, Gamma-ray induced effect on the structural and optical properties and durability of neodymium-doped zinc-bismuth-borotellurite glasses and glass ceramics, *Opt. Mater.*, 2023, **137**, 113572.

5 K. Wu, F. Wang, Q. Liao, H. Zhu, D. Liu and Y. Zhu, Synthesis of pyrochlore-borosilicate glass-ceramics for immobilization of high-level nuclear waste, *Ceram. Int.*, 2020, **46**(5), 6085–6094.

6 M. Y. Hanfi, A. K. Sakr, A. Ismail, B. M. Atia, M. S. Alqahtani and K. Mahmoud, Physical characterization and radiation shielding features of $B_2O_3As_2O_3$ glass ceramic, *Nucl. Eng. Technol.*, 2023, **55**(1), 278–284.

7 H. A. Fakhouri, B. Abughazaleh and M. Sayyed, Comparative evaluation of cubic spline, akima, and PCHIP interpolation methods for predicting radiation shielding parameters of heavy metal oxide glasses: numerical approximation for lead borate-based glasses using cubic splines, piecewise cubic hermite interpolating polynomial and akima interpolation, *Nucl. Eng. Technol.*, 2026, 104232.

8 H. Al-Ghamdi, N. Alfryyan, N. A. Alsaif, A. Abdelghany, K. Higazy, A. Abouhaswa, Y. S. Rammah, K. M. Kaky, A. J. Kadhim and F. El-Agawany, Impact of TiO_2-doped bismuth-boro-tellurite glasses: fabrication, physical and optical properties, and γ-ray protection competence for optical and radiation shielding applications, *J. Electron. Mater.*, 2025, **54**(2), 1432–1443.

9 M. R. Ahmed, N. A. Alsaif, N. Siddiqui, A. S. Prasad, M. Srinivas, S. K. Ahmmad, K. M. Kaky, A. J. Kadhim and Y. Rammah, Physical, thermal properties, FTIR and Raman spectroscopies as well as γ-ray attenuation capacity of borate glasses doped with Mn^{2+} ions: role of CaO/Al_2O_3 substitution, *Opt. Mater.*, 2025, **158**, 116461.

10 N. A. Alsaif, N. Alfryyan, H. Al-Ghamdi, A. Abdelghany, A. Abouhaswa, A. J. Kadhim, K. M. Kaky and Y. Rammah, Fabrication, structural, physical, optical characteristics and γ-ray attenuation capacity of borosilicate glasses doped with Gd_2O_3, *Sci. Rep.*, 2024, **14**(1), 30587.

11 M. Sayyed, M. Mhareb, K. M. Kaky, K. Mahmoud, A. J. Kadhim and Y. Maghrbi, Developing GTB glass system doped holmium oxide for radiation absorption and optical applications, *J. Sci.: Adv. Mater. Devices*, 2025, **10**(2), 100872.

12 A. Acikgoz, I. Izguden, Y. Tasgin, D. Yilmaz, G. Demircan, S. Kalecik and B. Aktas, Influence of praseodymium oxide on the structural, mechanical and photon, charged particles, and neutron shielding properties of alumina borate glass, *Ceram. Int.*, 2024, **50**(19), 34573–34584.

13 M. Sayyed, M. Mhareb, M. K. Hamad, A. J. Kadhim, H. Alsafi, K. Mahmoud and K. M. Kaky, Effects of MoO_3 on the structural, physical, mechanical, optical, and ionizing shielding of borate-germanate-telluride glass system, *Ceram. Int.*, 2024, **50**(22), 46008–46017.

14 M. Sayyed, M. Mhareb, K. M. Kaky, K. Mahmoud and A. J. Kadhim, A new approach toward enhancing the gamma-ray shielding efficiency: Zn ions effects on synthesized B_2O_3–PbO–BaO toward gamma-ray protection applications, *Ann. Nucl. Energy*, 2025, **210**, 110860.

15 R. I. Mahdi, M. Y. Hanfi, M. Mhareb, M. Sayyed, A. J. Kadhim and K. M. Kaky, Transparent heavy-metal glass-ceramics reinforced with nano-PbO for next-generation X-and γ-ray shielding applications, *Mater. Res. Bull.*, 2025, 113808.

16 M. Mhareb, M. K. Hamad, R. I. Mahdi, M. Sayyed, H. Mansour, A. J. Kadhim and K. M. Kaky, Tailoring the optical, mechanical, and gamma-ray-attenuation performance of GTB glasses by doping nano rare-earth (Gd, Yb, Tm), *Radiat. Phys. Chem.*, 2025, **237**, 113019.

17 V. Gupta, S. Kumar, S. Arya, R. Mishra and K. Singh, *et al.*, Blue-to-white light generation using rare-earth dopants and magnesium phosphate glass host interaction, *Opt. Mater.*, 2026, **174**, 117898.

18 M. Sayyed, M. Mhareb and K. M. Kaky, Characterization of mechanical and radiation shielding features of borosilicate glasses doped with MoO_3, *Silicon*, 2024, **16**(5), 1955–1965.

19 J. Thumma and R. K. Guntu, Design and evaluation of TiO_2-enhanced phosphate glasses for dual-functionality: photonic applications and radiation safety, *Phys. B*, 2025, 417735.

20 M. A. Imheidat, M. KhHamad, K. Naseer, M. Sayyed, N. Dwaikat, K. Cornish, Y. Alajerami, M. Alqahtani and M. Mhareb, Radiation shielding, mechanical, optical, and structural properties for tellurite glass samples, *Optik*, 2022, **268**, 169774.

21 P. Kaur, D. Singh and T. Singh, Heavy metal oxide glasses as gamma rays shielding material, *Nucl. Eng. Des.*, 2016, **307**, 364–376.

22 A. Mostafa, H. M. Zakaly, S. Al-Ghamdi, S. A. Issa, M. Al-Zaibani, R. Ramadan and E. El Agammy, PbO–Sb_2O_3–B_2O_3–CuO glassy system: evaluation of optical, gamma and neutron shielding properties, *Mater. Chem. Phys.*, 2021, **258**, 123937.

23 M. Sayyed, M. Mhareb, M. K. Hamad, A. J. Kadhim, K. M. Kaky and Y. Maghrbi, Structural, physical, optical, mechanical, and radiation shielding investigation of tantalum pentoxide doped germanate-tellurite–borate based glass system, *Results Phys.*, 2025, **75**, 108356.

24 M. Sayyed, K. M. Kaky, M. Mhareb, A. Al-keisy and S. Baki, Impact of cuo on TeO_2–GeO_2–ZnO–Al_2O_3–MgO glass system for ionizing shielding applications, *J. Mater. Sci.: Mater. Electron.*, 2023, **34**(36), 2277.

25 M. Hamad, N. Dwaikat, M. Mhareb, M. Sayyed, R. Hamad, Y. Alajerami, M. Almessiere, G. Saleh, A. H. Alomari and K. Ziq, Influence of erbium on structural, and charged particles, photons, and neutrons shielding properties of $Ba_{1-x}Er_xSnO_3$ perovskite ceramics, *J. Rare Earths*, 2024, **42**(4), 724–732.

26 A. T. Patel and A. Pratap, Study of kinetics of glass transition of metallic glasses, *J. Therm. Anal. Calorim.*, 2012, **110**(2), 567–571.

27 A. M. Al-Baradi, E. A. Wahab and K. S. Shaaban, Preparation and characteristics of B_2O_3–SiO_2–Bi_2O_3–TiO_2–Y_2O_3 glasses and glass-ceramics, *Silicon*, 2022, **14**(10), 5277–5287.

28 M. Kaur, G. Kaur, O. Pandey, K. Singh and V. Kumar, Influence of CaO/MgO ratio on the crystallization kinetics and interfacial compatibility with crofer 22APU and YSZ of strontium based alumino-borosilicate glasses for SOFC applications, *Int. J. Hydrogen Energy*, 2017, **42**(25), 16244–16257.

29 S. Khan, S. Kumar, N. Jast, K. Abida, K. Singh and S. Singh, Luminescence, mechanical and non-isothermal crystallization kinetics properties of MnO-doped borosilicate glasses for photonics applications, *J. Solid State Chem.*, 2025, 125608.

30 R. K. Guntu, P. Ashok, K. Sivaram, P. B. Shetty, S. Babu and M. Israr, Investigations on thermoluminescence, photoluminescence and radiation shielding properties of Dy_2O_3 doped Li_2O–Al_2O_3–SiO_2–Y_2O_3 glasses for thermoluminescent dosimeter applications, *Appl. Phys. A*, 2025, **131**(9), 701.

31 A. Makishima and J. D. Mackenzie, Direct calculation of Young's modulus of glass, *J. Non-Cryst. Solids*, 1973, **12**(1), 35–45.

32 A. A. El-Rehim, H. Zahran, I. Yahia, S. A. Makhlouf and K. S. Shaaban, Radiation, crystallization, and physical properties of cadmium borate glasses, *Silicon*, 2021, **13**(7), 2289–2307.

33 H. Doweidar, Consideration of the boron oxide anomaly, *J. Mater. Sci.*, 1990, **25**(1), 253–258.

34 B. Bridge and A. Higazy, A model of the compositional dependence of the elastic moduli of polycomponent oxide glasses, *Phys. Chem. Glasses*, 1986, **27**(1), 1–14.

35 B. Bridge, N. Patel and D. Waters, On the elastic constants and structure of the pure inorganic oxide glasses, *Phys. Status Solidi A*, 1983, **77**(2), 655–668.

36 O. H. Abd-Elkader, M. Nasrallah, M. Nasrallah, S. Aleya, M. O. Abdelkader and A. Saleh, Rapid fabrication, magnetic, and radiation shielding characteristics of $NiFe_2O_4$ nanoparticles, *Opt. Mater. Express*, 2024, **14**(5), 1170–1185.

37 A. Saleh, Comparative shielding features for X/gamma-rays, fast and thermal neutrons of some gadolinium silicoborate glasses, *Prog. Nucl. Energy*, 2022, **154**, 104482.

38 S. A. Saleh, S. Tajudin, M. Algethami, K. T. Osman, K. Said, A. S. Elshoukrofy and T. Y. Wais, Fatma elzahraa mansour, optimizing the integration between radiation protection, optical, and mechanical strength for advanced nuclear safety applications using tungsten-doped bismuth borate glasses, *Radiat. Phys. Chem.*, 2026, **238**, 113216.

39 N. A. Abdelhakim, R. M. Shalaby, A. Abdelghany, M. Mitwalli, A. El-Farrash and A. Saleh, Integration between radiation shielding performance, structural evolution, and mechanical features of co-doped sodium phosphate glasses, *Sci. Rep.*, 2026, **16**, 1958.

40 A. Saleh, A. Kobyliukh, N. Basfer, S. Tajudin and U. Szeluga, Comprehensive examination of synthesis, microstructure, and radiation shielding effectiveness of multi-layered polymeric GNP-nanocomposites, *Radiat. Phys. Chem.*, 2025, **237**, 113078.

41 E. Sakar, Ö. F. Özpolat, B. Alm, M. Sayyed and M. Kurudirek, Phy-X/PSD: development of a user friendly online software for calculation of parameters relevant to radiation shielding and dosimetry, *Radiat. Phys. Chem.*, 2020, **166**, 108496.

42 N. Alharbiy, Z. Khattari, Y. Rammah and A. Saleh, Role of Al_2O_3, WO_3, Nb_2O_5, and PbO on the physical, elasto-mechanical and radiation attenuation performance of boro-tellurite glasses, *J. Mater. Sci.: Mater. Electron.*, 2023, **34**(3), 191.

43 J. Kaur, S. Kumar, I. Mudahar and K. Singh, Tunable green-blue luminescence of Dy_2O_3 doped borosilicate glasses for optoelectronic devices, *J. Mol. Struct.*, 2025, **1322**, 140574.

44 L. U. Grema, S. Kumar, S. Khan, K. Singh and S. Umar, Thermo-mechanical, structural and electrical properties of Ba–La–Zn–Al-borosilicate glasses as sealants for application in SOFCs, *J. Non-Cryst. Solids*, 2026, **671**, 123826.

45 A. Abd El-Moneim, Bond compression bulk modulus and Poisson's ratio of the polycomponent silicate glasses, *Mater. Chem. Phys.*, 2001, **70**(3), 340–343.

46 S. Kumar, S. Thakur, P. K. Jha, D. Kumar and K. Singh, Conversion of cool-to-warm orange-reddish light emitting diode by Sm2O3 addition in magnesium borosilicate glasses, *J. Mol. Struct.*, 2024, **1312**, 138432.

47 S. Khan, S. Kumar, G. Singla, K. Singh and P. K. Jha, Tuning crystallization, strength, and luminescence property of CuO modified sodium-phosphate glasses, *ECS J. Solid State Sci. Technol.*, 2025, **14**(8), 086004.

48 S. Kumar, K. Singh and D. Kumar, B_2O_3 anomaly effect on crystallization and mechanical properties of soda-lime silicate glasses, *Mater. Today Commun.*, 2024, **39**, 109247.

49 C. Bernard, S. Chaussedent, A. Monteil, M. Montagna, L. Zampedri and M. Ferrari, Simulation by molecular dynamics of erbium-activated silica-titania glasses, *J. Sol-Gel Sci. Technol.*, 2003, **26**(1), 925–929.

50 M. Halimah, W. Daud and H. Sidek, Elastic properties of TeO_2–B_2O_3–Ag_2O glasses, *Ionics*, 2010, **16**(9), 807–813.

51 S. Inaba, S. Oda and K. Morinaga, Heat capacity of oxide glasses at high temperature region, *J. Non-Cryst. Solids*, 2003, **325**(1–3), 258–266.

52 R. El-Mallawany, Tellurite glasses part 1. elastic properties, *Mater. Chem. Phys.*, 1998, **53**(2), 93–120.

53 D. Souri, Fragility, DSC and elastic moduli studies on tellurite-vanadate glasses containing molybdenum, *Measurement*, 2011, **44**(10), 1904–1908.

54 S. Khan, S. Kumar, S. Khan, K. Abida and K. Singh, Influence of ZrO_2 on non-isothermal crystallization kinetics, structure and optical properties of calcium borosilicate glasses, *Mater. Today Commun.*, 2024, **40**, 109526.

55 S. Khan, S. Kumar, K. Abida and K. Singh, Non-isothermal crystallization kinetics, optical and structural properties of MgO-doped vanadate glasses, *J. Therm. Anal. Calorim.*, 2024, **149**(11), 5299–5311.

56 I.-C. Chen, P.-Y. Lin, T. T. Li and J.-Y. Chang, Kinetic study of the thermal crystallization behavior of hydrogenated amorphous silicon prepared by ECRCVD, *ECS J. Solid State Sci. Technol.*, 2014, **3**(5), N75.

57 H. E. Kissinger, *et al.*, Variation of peak temperature with heating rate in differential thermal analysis, *J. Res. Natl. Bur. Stand*, 1956, **57**(4), 217–221.

58 J. Augis and J. Bennett, Calculation of the avrami parameters for heterogeneous solid state reactions using a modification of the kissinger method, *J. Therm. Anal.*, 1978, **13**(2), 283–292.

59 A.-M. Hu, K.-M. Liang, M. Li and D.-L. Mao, Effect of nucleation temperatures and time on crystallization behavior and properties of Li_2O–Al_2O_3–SiO_2 glasses, *Mater. Chem. Phys.*, 2006, **98**(2–3), 430–433.

60 S. Danewalia, K. Singh and S. Arya, Influence of vanadium oxide on non-isothermal crystallization kinetics of zinc lithium borate glasses, *J. Non-Cryst. Solids*, 2021, **553**, 120471.

61 R. Iordanova, E. Lefterova, I. Uzunov, Y. Dimitriev and D. Klissurski, Non-isothermal crystallization kinetics of V_2O_5–MoO_3–Bi_2O_3 glasses, *J. Therm. Anal. Calorim.*, 2002, **70**(2), 393–404.

62 D. L. Sidebottom, Connecting glass-forming fragility to network topology, *Front. Mater.*, 2019, **6**, 144.

63 O. A. Lafi and M. M. Imran, Compositional dependence of thermal stability, glass-forming ability and fragility index in some Se–Te–Sn glasses, *J. Alloys Compd.*, 2011, **509**(16), 5090–5094.

64 T. Mel'Nichenko, V. Rizak, T. Mel'Nichenko and V. Fedelesh, Parameters of the fluctuation free volume theory for glasses in the Ge–As–Se system, *Glass Phys. Chem.*, 2004, **30**(5), 406–414.

65 M. Sayyed, M. K. Hamad and M. Mhareb, Radiation shielding properties for a borosilicate glass: role of varying PbO, *Opt. Mater.*, 2025, **159**, 116602.

66 A. Ratep, A. Abdelaziem, M. Hanfi, K. Mahmoud and I. Kashif, Enhancing gamma-ray shielding with bismuth oxide-infused boron oxides, *Opt. Quantum Electron.*, 2024, **56**(2), 143.

67 H. Yilmaz Alan, Efficacy of barium and calcium additives in lithium silicate glasses for nuclear shielding applications, *Phys. Scr.*, 2024, **99**(7), 075314.

68 M. Sayyed, A. Bennal, M. Y. Hanfi, V. K. Bhovi and S. A. Issa, *et al.*, Impact of Y_2O_3 and Sm_2O_3 doping on the radiation shielding properties of lead-borate glasses, *Appl. Radiat. Isot.*, 2025, 112407.

69 A. H. Almuqrin, D. A. Aloraini, M. Sayyed and M. Alwehaibi, Structural and attenuation properties of rare-earth and barium oxide modified borate glasses for gamma ray protection, *Open Chem.*, 2026, **24**(1), 20250223.

70 J. Budida, C. S. Rao, N. R. Chand and R. K. Guntu, Spectral and structural tailoring of Sm_2O_3-doped LiF–La_2O_3–PbO–B_2O_3 glasses for advanced luminescent devices, *J. Electron. Mater.*, 2025, **54**(11), 10611–10647.

71 K. Boonin, P. Yasaka, P. Yamchumporn, N. Triamnak, S. Kothan and J. Kaewkhao, Scintillation respond and orange emission from Sm^{3+} ion doped tellurite and fluorotellurite glasses: a comparative study, *Radiat. Phys. Chem.*, 2021, **189**, 109754.

72 B. Burtan-Gwizdala, J. Cisowski, R. Lisiecki, K. J. Kowalska, B. Jarzabek, N. Nosidlak, M. Reben, A. M. Alshehri, K. I. Hussein and E. S. Yousef, Thermal, optical, and emission traits of Sm^{3+}-ion-doped fluoride/chloride/oxide glass for red/orange laser fiber applications, *Fibers*, 2024, **12**(11), 100.

73 B. Swetha, A. P. Chowdhury and M. Kokila, Sodium lanthanum boro-tellurite glasses with Sm^{3+} ion doping and gold nanoparticle embedding: a new glass matrix for solid state lighting devices, *J. Alloys Compd.*, 2025, **1010**, 177628.

74 S. Ghosh, J. Biswas and S. Jana, Deciphering the role of CIElab on emission mechanism of samarium (Sm^{3+}) ions embedded boro-tellurite glasses for applications in optoelectronics devices, *Phys. B*, 2025, **699**, 416819.

75 K. Sudhakar Reddy, Influence of samarium concentration on the luminescence characteristics of lithium borate glasses for reddish-orange emission applications, *Int. J. Curr. Sci.*, 2025, **15**(5), 355–363.

76 P. Aruna, S. Hajira, M. V. Ramanaiah, V. S. Reddy, K. N. Reddy and B. S. Reddy, Optical analysis of Eu^{3+} and Tb^{3+}: B_2O_3–P_2O_5–WO_3–Li_2O–(ZnO/CdO/TeO_2) glasses, *Next Mater.*, 2025, **8**, 100703.

77 K. Bansal, N. K. Mishra, I. Abdullahi, P. J. Singh, M. Tyagi and S. Singh, Studies of luminescence traits and judd-ofelt analysis of Sm^{3+} activated oxyfluoride glasses, *Opt. Mater.*, 2024, **147**, 114579.

78 S. Mahamuda, F. Syed, C. B. A. Devi, K. Swapna, M. Prasad, M. Venkateswarlu and A. Rao, Spectral characterization of Dy^{3+} ions doped phosphate glasses for yellow laser applications, *J. Non-Cryst. Solids*, 2021, **555**, 120538.

79 A. Florez, V. Jerez and M. Florez, Optical transitions probabilities of Dy^{3+} ions in fluoroindate glass, *J. Alloys Compd.*, 2000, **303**, 355–359.

80 B. R. Judd, Optical absorption intensities of rare-earth ions, *Phys. Rev.*, 1962, **127**(3), 750.

81 G. Ofelt, Intensities of crystal spectra of rare-earth ions, *J. Chem. Phys.*, 1962, **37**(3), 511–520.

82 J. S. Kumar, K. Pavani, A. M. Babu, N. K. Giri, S. Rai and L. R. Moorthy, Fluorescence characteristics of Dy^{3+} ions in calcium fluoroborate glasses, *J. Lumin.*, 2010, **130**(10), 1916–1923.